Bulletin of Earthquake Engineering
https://doi.org/10.1007/s10518-026-02476-y

ORIGINAL ARTICLE

Sequence-aware Damage Accumulation Function for light damage in masonry walls under repeated, nonidentical earthquakes

Paul A. Korswagen[1] · Jan G. Rots[1]

Received: 18 June 2025 / Accepted: 14 April 2026

Abstract

Decades of induced seismicity in Groningen have exposed unreinforced clay masonry to frequent, shallow, small-to-moderate earthquakes. Conventional, event-centric vulnerability assessments largely ignore the cumulative effects of repeated shaking and therefore under-predict visible (light, crack-based) damage. We propose a sequence-aware Damage Accumulation Function (DAF) that advances a measured crack-based state Ψ across arbitrary PGV histories by separating similar-intensity repetitions (small increments) from events that set a new maximum (disproportionate jumps). The method integrates (i) earlier full-scale wall and spandrel experiments with high-resolution digital image correlation to quantify crack initiation, widening and extension; (ii) earlier calibrated nonlinear time-history analyses of Groningen-type motions using the Engineering Masonry Model; and (iii) a semi-empirical surrogate linking $\Delta\Psi$ to PGV and typological parameters with heteroskedastic, PGV-dependent uncertainty whose incremental contribution decays with sequence position. Applied to historical records and hypothetical futures, DAF results indicate that repeated low-intensity events meaningfully affect accumulation (≈10–20% additional $\Delta\Psi$ for same-intensity repeats), while a record-high PGV produces a marked jump. Regional analyses yield exceedance maps that differ from single-event fragility, especially at the edges with low but repeated PGV values and enable decision-facing metrics such as "damage hastening." The formulation is intended for DS1/early DS2 crack damage of in-plane URM walls and uses PGV as the intensity measure. The DAF provides an interpretable, probabilistic complement to standard fragility where history and repetition govern light-damage progression.

Keywords Clay masonry · Light damage · Cracks · Vulnerability · Fragility

✉ Paul A. Korswagen
p.a.korswagen@tudelft.nl

[1] Department of Materials, Mechanics, Management and Design, Faculty of Civil Engineering and Geosciences, Delft University of Technology, Delft, The Netherlands

1 Introduction

Induced seismicity associated with decades of gas extraction in the Groningen field has subjected a predominantly unreinforced-masonry (URM) building stock to frequent, shallow, small-to-moderate events. Region-specific Ground Motion Prediction Equations (GMPEs) for Groningen, together with short-distance formulations for small-to-moderate events, consistently indicate short-period motions that are modest compared with tectonic earthquakes but still energetic enough to open and widen cracks in brittle, low-tension masonry, especially when such motions repeat (Bommer et al. 2017; Atkinson 2015; Suzuki and Iervolino 2017; Zöller and Holschneider 2016; Sarhosis et al. 2021). In this Dutch context, multi-scale studies have documented characteristic crack patterns and damage trajectories for fired-clay and calcium-silicate masonry and their consequences for durability, perceived safety, and residual stiffness/strength (Jafari and Esposito 2016; Messali et al. 2018; Esposito et al. 2019; Grottoli et al. 2019; Kvande and Lisø 2009). Socio-economic research shows tangible impacts of even “light” shaking on quality of life and property markets, which in turn motivated risk policies up to and including closure of the Groningen field (Boelhouwer and van der Heijden 2018; van der Voort and Vanclay (2015; Mulder et al. 2018; Stroebe et al. 2021; van Elk et al. 2019).

Repetition, rather than a single “largest” event, is the defining feature for light, crack-based damage in Groningen. Administrative practice has often used ~2 mm/s PGV as a claim threshold, and local histories show many exceedances over recent decades, i.e., many opportunities for incremental crack advance at low drift (Bommer et al. 2017, wetten.overheid.nl, 2023). Figure 1 illustrates this repetition explicitly: a time history of PGV at Loppersum with all exceedances of 2 mm/s highlighted, emphasizing that small events recur far more often than strong ones and thus dominate cumulative light damage. Laboratory and field evidence in Dutch masonry confirm that visible cracks can initiate near these levels, especially when boundary conditions are unfavourable or pre-existing defects (pre-damage)

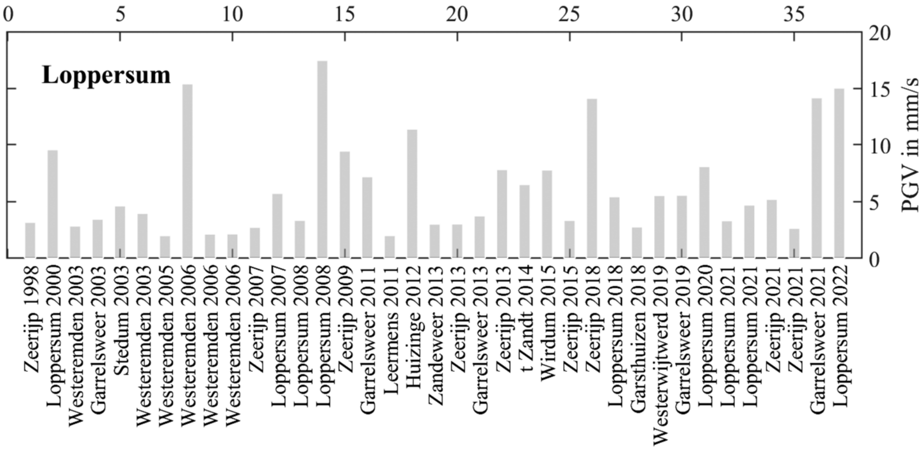

Fig. 1 Repetition of PGV—events from 1990 to 2024 at Loppersum with PGVs above 2 mm/s. The value of 2 mm/s in this graph corresponds to the 75% exceedance probability (a 25% probability of exceedance) determined with the ground motion prediction Equations (GMPEs) of Bommer et al. (2019). The figure shows that a PGV of 5 mm/s is exceeded at least ten times

provide a focus for crack propagation (Jafari and Esposito 2016; Van Staalduinen et al. 2018; Lagomarsino et al. 2013; Korswagen et al. 2019a, 2019b, 2020b, 2020a, 2025).

The Groningen-related literature has tried to fold repeated (or “recursive”) shaking into assessment in several ways (Mouyiannou et al. 2014; Sokolkin et al. 1998; Dais et al. 2017; Dais 2021). Portfolio-scale studies combine induced-seismicity hazard with typology-based fragility and consequence models to quantify risk and explore mitigation (Crowley et al. 2017, 2019; van Elk et al. 2019). Sequence-specific nonlinear finite-element (NLFE) simulations for representative façades examine how successive events accelerate cracking and stiffness loss (Sarhosis et al. 2019a, 2019b; Grant et al. 2019). These methods agree on two DS1-relevant points: many small repeats matter as they “nudge” cracks forward and, a new event that exceeds all earlier intensities produces a disproportionate jump. Yet most workflows remain event-centric (“memoryless”), conditioning damage on either the maximum intensity or distributions that ignore order and prior cracking, which under-predicts visible damage where dozens of small events accumulate (Grünthal et al. 1998; Lagomarsino et al. 2013; Lovon et al. 2018; Crowley et al. 2019).

To move beyond event-wise thinking, various approaches explicitly consider repetition, fatigue, or aggravation (Melnikov and Semenov 2014; Mkrtychev and Lokhova 2021; Sandoval et al. 2017; Katsimpini et al. 2025; Liu et al. 2024a, 2024b, 2025; Esteva et al. 2016). In Groningen-oriented work, proxies include cycle-counting modifiers on drift measures, phenomenological degradation indices fitted to NLFE results, envelope rules that treat a “record-breaking” event differently from a same-intensity repeat, and time-in-state formulations (Sarhosis et al. 2019a, 2019b; Grant et al. 2019; Iervolino et al. 2016). Related fields contribute order- and history-sensitive ideas: nonlocal damage and damage-plasticity for masonry elements (Toti et al. 2015), classical and stochastic fatigue accumulation (Schijve 1972; Lutes et al. 1984; Gusella 1998; Lepov 2013; Zhu et al. 2017; Lv et al. 2015; Wu et al. 2019), data-driven deterioration models (Li et al. 2019; Yan et al. 2020; Cristiani et al. 2021; Samadian et al. 2025; Gao et al. 2025), and cumulative-sequence modelling for RC buildings (Wu et al. 2021; Oyguc et al. 2023). These frameworks share two features valuable to URM at DS1: a state variable that carries memory between loadings, and an update rule that distinguishes similar-amplitude repetition from steps to a new maximum. Analogies from the RC/infilled-frame literature are instructive. Under repeated drifts, RC and masonry-infilled frames exhibit pinching, stiffness and strength decay, and pronounced sequence effects that cannot be captured by a single-event check, reinforcing the need for a state-updating approach (Wu et al. 2021; Oyguc et al. 2023; Filippou et al. 2019). Other sources highlight additional inspiration: for example, (Nie et al. 2024), looked at the accumulation of damage on transmission towers.

Masonry’s own micromechanics (fracture and sliding at brick-mortar interfaces, crack coalescence, and, depending on unit-mortar relationships like for calcium-silicate masonry, unit-splitting) explain why small repeats accumulate visible damage even when peak drift does not increase (Jafari and Esposito 2016; Shadlou et al. 2020; Luciano and Sacco 1998). Recent Groningen-calibrated campaigns used high-resolution DIC to quantify within-step crack growth at constant drift and to define a reproducible, crack-based scalar Ψ that aggregates crack number, length and width, providing a common measure across experiments, models, and field observations (Korswagen et al. 2019a, 2019b, 2020b, 2025). These tests showed direction-dependent force degradation after one-way cycling and steeper Ψ growth in calcium-silicate than in fired-clay at the same drift, supporting that repeated “small” events remain consequential (Korswagen et al. 2020b, 2025).

In the field, several monitoring techniques have been investigated to assess the evolution of damage (Sangirardi et al. 2022; Lu et al. 2020; Rezaie et al. 2022), but few focus on small, barely visible cracks (Shettya et al. 2019; Massart et al. 2007). Moreover, (Vanniamparambil et al. 2014) looked at quantifying progressive damage on reinforced concrete and masonry walls, while (Shi et al. 2024) observed damage during explosion tests. In these cases, the increase in damage was measured during load repetitions.

On the computational side, continuum-modelling approaches for in-plane URM have matured and been benchmarked, enabling Groningen-specific calibration against crack patterns and hysteresis, albeit with ongoing development toward explicit cyclic-degradation laws in constitutive models (Schreppers et al. 2016; Bindiganavile-Ramadas 2018; D’Altri et al. 2020). Groningen-calibrated nonlinear time-history analyses (NLTHA) incorporate soil–structure interaction (SSI), façade typology, and pre-damage to produce crack-based fragility curves as functions of PGV, highlighting the influence of initial condition and site effects (Longo et al. 2021; Korswagen et al. 2022; Gazetas 1991). At building and façade scales, settlement-induced damage studies independently corroborate progressive cracking when long-term ground movements and repeated light earthquakes act together (Burland and Wroth 1974; Amorosi et al. 2014; Prosperi et al. 2023, 2025). Diagnostic and pattern-based schemes emphasize that crack topology governs residual stiffness and perceived damage, implying that any scalar metric should be used with awareness of its limits (de Vent 2011; Latifi et al. 2023; Dolatshahi and Beyer 2022). Masonry-targeted damage accumulation assessments outside Groningen are emerging as well (García de Quevedo Inarritu et al. 2024), and broader multi-hazard syntheses echo the need to track a damage state across sequences (Zhang et al. 2024).

In summary, the literature provides four ingredients for accumulation in URM: portfolio methods that are efficient but largely memoryless (Lagomarsino et al. 2013; Crowley et al. 2017; Grünthal et al. 1998; Lovon et al. 2018); sequence-specific NLFE studies that are physics-rich yet case-by-case (Sarhosis et al. 2019; Grant et al. 2019); cumulative-damage proxies from fatigue and nonlocal damage that carry memory and respect order (Iervolino et al. 2016; Toti et al. 2015; Schijve 1972; Lutes et al. 1984; Gusella 1998; Lepov 2013; Zhu et al. 2017; Lv et al. 2015; Wu et al. 2019); and data-driven surrogate and uncertainty quantification (UQ) tools that scale predictions probabilistically (Yan et al. 2020; Cristiani et al. 2021; Samadian et al. 2025; Gao et al. 2025). What has been missing is a mechanics-informed, sequence-aware rule that (a) advances a crack-based state variable between events, (b) distinguishes similar-intensity repeats from “record-breaking” events, and (c) propagates uncertainty coherently over long, heterogeneous PGV histories.

This paper addresses that gap by proposing a Damage Accumulation Function (DAF) tailored to crack-based light damage in masonry. The formulation adopts Ψ as the carried damage state, uses a surrogate damage function calibrated on Groningen-relevant NLTHA to map intensity and parameters to incremental damage, and introduces a similarity ratio to separate repetition at comparable intensity from steps to a new maximum, mirroring observed “small-increment” versus “jump” behaviour (Korswagen et al. 2019a, 2019b, 2020b, 2022; Longo et al. 2021). Uncertainty is included via a PGV-dependent term whose contribution diminishes with sequence position, preventing over-dispersion in long histories while recognizing the larger variability of higher-intensity events. The framework admits arbitrary, heterogeneous PGV histories generated from region-specific GMPEs or local measurements and naturally incorporates initial condition, SSI, and multi-hazard influences, providing a way to quantify "damage hastening" where repeated light earthquakes accelerate damage that would otherwise have taken longer to occur due to, for instance, settlement-type actions.

In this way, this paper marks the culmination of a multi-step programme aimed first at observing and quantifying light-damage crack mechanisms and repetition effects in full-scale walls and spandrels, then at reproducing those mechanisms in calibrated macro- or continuum-models, and finally at incorporating sequence effects into a transferable function that updates Ψ across real PGV histories. The background experimental and computational studies that anchor Ψ, establish drift windows for light damage, and calibrate the modelling strategy, are reviewed in Sect. 2 (Jafari and Esposito 2016; Messali et al. 2018; Esposito et al. 2019; Grottoli et al. 2019; Korswagen et al. 2019a, 2019b, 2025; Schreppers et al. 2016; D'Altri et al. 2020). Sect. 3 introduces the DAF, detailing its two-branch update (similar-intensity repeats vs. new-maximum events) and the uncertainty propagation. Section 4 applies the method to historical Groningen sequences and scenario-based futures, illustrating regional exceedance patterns and "damage hastening", while Sect. 4 includes an extended discussion. Figure 2 summarises the overall workflow: from experiments to calibrated modelling (including SSI per (Gazetas 1991)), the surrogate Ψ(·), the DAF, and its applications, so that the reader can follow how each element informs the next.

2 Background studies

Several earlier studies have investigated crack initiation and propagation in masonry structures using a physical approach (Korswagen et al. 2019a, 2019b, 2020b, 2020a, 2025; Korswagen and Rots 2020; Longo et al. 2021; Korswagen et al. 2022). That means, experiments and models have been used to investigate cracking instead of solely analysing damage reports from existing structures (Prosperi et al. 2023). While observational data can highlight the presence of damage, it often lacks consistency, objectivity, and insight into the underlying mechanisms of crack initiation and propagation (Jafari and Esposito 2016; de Vent 2011). In contrast, controlled laboratory testing enables a deeper understanding of how cracks form and evolve under repeated loading conditions. The studies have employed a dimensionless damage parameter (Ψ) that quantifies cracking in terms of number, length, and width of cracks (see Eq. 1), offering a reproducible and scalable measure of damage severity (Korswagen and Rots 2020). This parameter, unlike subjective assessments from damage reports, allows for direct comparison between specimens and facilitates the calibration of finite element models that can simulate more complex loading scenarios. Moreover, the experimental approach reveals important phenomena such as material degradation and damage accumulation, which are difficult to discern from observational data alone. By linking observed damage directly to structural drift and mechanical behaviour, the physics-based methodology not only improves predictive modelling but also provides a more reliable foundation for assessing damage progression.

$$\Psi = 2 \cdot n^{0.15} \cdot c_w^{0.3} \tag{1}$$

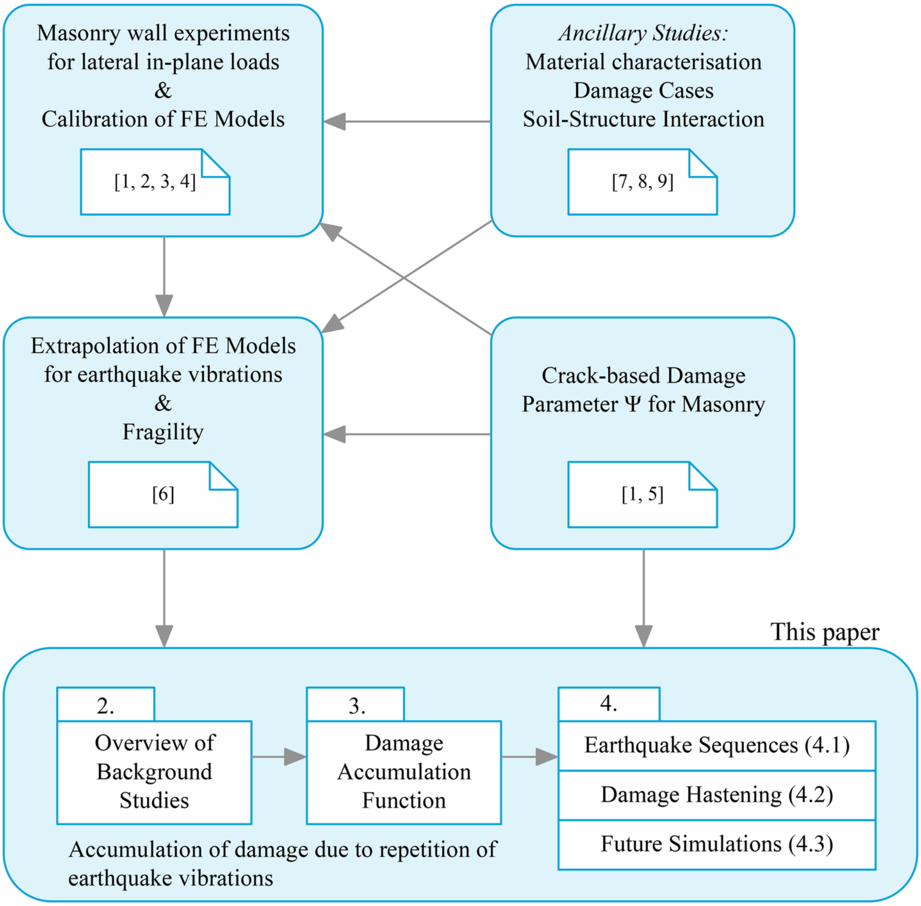

Fig. 2 Flowchart of entire study and sub-focus for this paper. Figure references in order 1–9 (Korswagen et al. 2019, 2020a, 2020b, 2025; Korswagen and Rots 2020; Korswagen et al. 2022; Longo et al. 2021; Jafari and Esposito 2016; Van Staalduinen et al. 2018)

$$c_w = \frac{\sum_{i=1}^{n} c_i^2 \cdot L_i}{\sum_{i=1^n} c_i \cdot L_i} \tag{1.a}$$

$$c_i = \sqrt{c_o^2 + c_s^2} \tag{1.b}$$

where c_i is the maximum crack width of crack i with both its opening (co) and sliding (cs) components, L_i is its length, and n is the total number of cracks present. The maximum crack width of each crack is composed by the opening and sliding components.

This section will briefly present earlier, related studies while focusing on the aspect of repeated loading. First, past wall experiments subjected to repeated loading will be introduced. Second, calibrated models to reproduce crack propagation will be detailed. Third, numerical models from (Korswagen et al. 2019), employed to conduct non-linear time-history analyses (NLTHA) and making use of the calibrated modelling strategies, are shown.

Finally, the surrogate model, relating earthquake intensity and building properties with damage from (Korswagen et al. 2022) is introduced.

2.1 Wall experiments

An extensive experimental campaign on full-scale masonry walls, about 3 m wide and 2.7 m tall, surveyed with high-resolution Digital Image Correlation and tested quasi-statically for in-plane drift, is the basis of the crack characterisation study (Korswagen et al. 2025). In these campaigns, full-field DIC was configured to resolve sub-0.1 mm crack openings and to convert displacement discontinuities into automated measures of crack width and length, enabling objective computation of the scalar crack-based damage parameter Ψ (combining number–length–width) at each loading increment (Korswagen et al. 2019a, 2019b). Figure 3 exemplifies the walls and shows how cracks, starting smaller than 0.1 mm in width, were automatically detected. The walls, varying in boundary conditions (cantilever or fixed), in geometry (with or without opening), and in material (fired-clay brick or calcium-silicate brick masonry) were tested under a repetitive, increasing protocol. Protocols deliberately included many small-amplitude repetitions within each step to emulate frequent light earthquakes and to reveal within-step accumulation; most tests used an initial one-way repetitive phase followed by two-way cyclic increments. In Fig. 3, the protocol shown includes three identical cycles (or repetitions) for every incremental step. Walls were tested with up to 100 repetitions per step with most walls being first subjected to a one-way cyclic load, without load reversal, before restarting with a two-way cyclic test. Companion spandrel tests complemented wall tests to isolate vertical cracking mechanisms and provide higher-resolution observations of unit splitting and CMOD-controlled accumulation (Crack Mouth Opening Displacement). Table 1 provides an overview of the tests; for additional details see (Korswagen et al. 2025).

Material contrasts and configurations were chosen to reflect Dutch practice. Fired-clay walls representative of pre-1950 masonry and calcium-silicate (CaSi) walls typical of 1970-modern inner leaves were both tested at full scale; tests on CaSi spandrels and walls showed stiff, slightly stronger initial response but more brittle light-damage behaviour than fired-clay at the same drift, with cracks frequently splitting bricks rather than following joints (Korswagen et al. 2020b). This mechanism contrast matters for visible/light damage: unit-splitting in CaSi produced fewer but wider cracks and more persistent residual openings, increasing perceived damage and repair intrusiveness relative to joint-following cracks in clay masonry.

The magnitude of the repeated drift is shown at the top of Fig. 4; tests were conducted below a drift of 0.1% which is associated with the type of cracks that would be expected at low earthquake intensities. This focus on sub-0.1% drift aligns with light-damage (DS1) regimes established in earlier clay-brick wall tests (≈0.3–1.1 ‰) and with later synthesis of upper light-damage thresholds, which places the end of the light-damage range well above the present test window (for fired-clay near ~0.5%, with CaSi exceeding light damage at ~40% lower drift). Figure 4 however, focuses on the degradation of the force required to enforce the prescribed drift. Since the experiments were displacement-controlled, the lateral force applied at the top of the wall was tuned to maintain certain displacements. This means that as the walls became damaged, their stiffness decreased and a subsequent repetition of an identical drift required the application of a lower force. Quantitatively, peak force

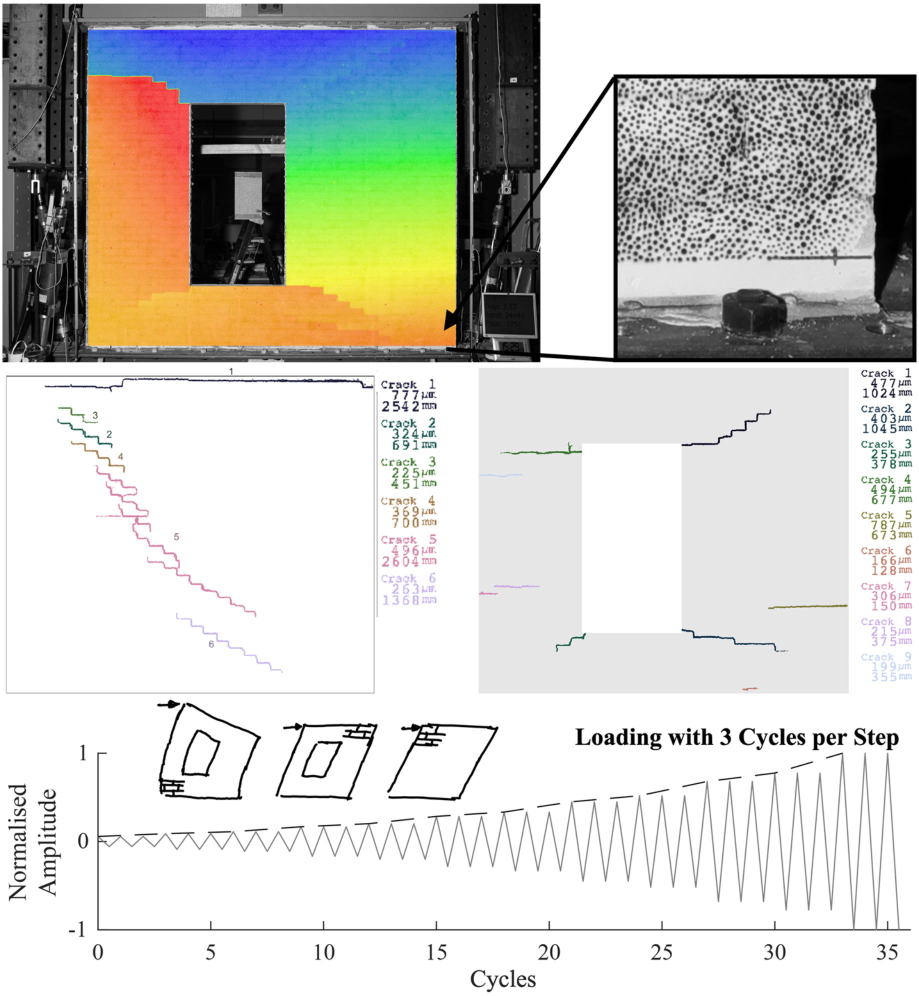

Fig. 3 Overview of experimental campaign. Top, wall with asymmetric opening painted with a speckle pattern for Digital image correlation showing the vertical displacement field overlaid in colour. Middle, automatic cracking detection from DIC for two other walls. Bottom, cyclic/repetitive loading protocol showing 3 cycles per incremental step, and sketch of different boundary conditions/wall types

typically reduced stepwise by a few percent per increment and, after an extended one-way repetitive phase, by as much as ~30% in the previously cycled direction, with most within-step degradation stabilising after ~30 repetitions. The degradation of the lateral force can be seen as an effect of repetition. In Figure 4 the progress of each wall shows how the force had to increase when the drift increased but subsequently decreased exponentially over the multiple repetitions. For two-way cycles, the negative direction displays the largest force degradation since the positive direction of the cycle had been tested during the one-way cyclic portion of the tests.

Since the drift was kept identical within each step, one would expect that cracking would not progress until the drift was increased. However, the experiments show that cracks propa-

Table 1 Summary of tested # walls and window banks used for calibration. Wall types A–F denote different experimental configurations (geometry, openings, boundary conditions); types A and B were used for NLTHA extrapolation (Fig. 7). Boundary codes: C=cantilever, F=fixed (double-clamped). For wall types see Korswagen et al. (2024)

Wall Name	Wall Type	Boundary	Year Built	Protocol		
				Repetitive	Cyclic	Near Collapse
Comp40	B	C	2017	5×3	7×50	81 mm
Comp41	B	C	2017	5×10	7×30	40 mm
Comp42	B	C	2017	6×20	7×30	40 mm
Comp43	B	C	2017	NA	7×50	40 mm
Comp44	B	C	2017	6×20	NA	NA
Comp45	C	C	2018	5×30	7×30	NA
Comp46	C	C	2018	5×30	7×30	81 mm
Comp47	A	F	2018	A 7×10		27 mm
Comp48	A	F	2018	A 7×10		NA
Comp49	E	C	2018	5×30	7×30	40 mm
Comp50	E	C	2018	5×30	7×30	40 mm
Comp51	E	C	2021	5×30	7×30	81 mm
Comp52	E	C	2021	5×30	7×30	81 mm
Comp53	E	F	2021	5×30	7×30	40 mm
Comp54	B	C	2021	5×30	5×30	NA
Comp55	B	F	2021	6×30	8×30	27 mm
Comp56	B	F	2021	5×30	7×30	27 mm
Comp57	D	F	2021	A 7×10		40 mm
Comp58	F	F	2021	A 7×10		67 mm
Comp59	F	F	2021	A 7×10		54 mm

gated within each step; the deformation of the walls thus was increasingly concentrated into cracking. Full-field DIC maps confirmed incremental widening and extension of a small set of dominant cracks during constant-drift repetitions, even when crack widths remained within DS1; corresponding force decay tracked this accumulation. This is displayed in Figure 5 where the crack-based damage intensity parameter Ψ is measured. Indeed, Ψ increases when drift is increased, but also within steps one can observe a change in Ψ. For the materials and geometries tested, Ψ rose more steeply with drift for CaSi than for fired-clay, consistent with unit-splitting and lower apparent fracture energy measured in CaSi spandrels; nevertheless, both materials exhibited within-step $\Delta\Psi$ under repetition. If the experiments had not been displacement- or drift-controlled, the reduction in stiffness would have resulted in a large increase in damage. Finally, boundary and configuration effects observed across the dataset (cantilever vs. double-clamped setups, shear walls vs. walls with openings) affected crack intensity at equal drift and should be accounted for when generalising accumulation trends beyond the figures shown here.

In summary for this subsection: the repeated-incremental protocols, high-resolution DIC, and the Ψ metric together captured (i) measurable within-step accumulation at constant drift, (ii) direction-dependent degradation after one-way cycling, and (iii) material-mechanism contrasts (unit-splitting vs. joint-following) that explain why nominally “small” repeated events can still advance light, crack-based damage, precisely the behaviour the Damage Accumulation Function later aims to reproduce and generalise.

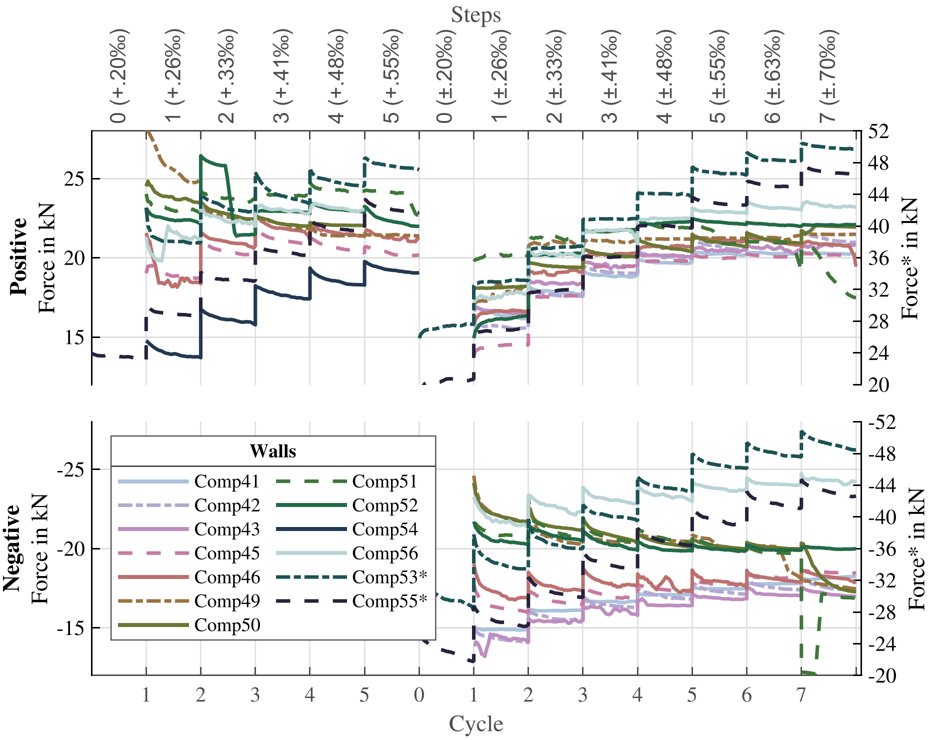

Fig. 4 Effect of repetition in experiments in terms of force reduction over cycles and steps. One way in-plane drift (up to +0.55‰) followed by two-way drift (up to ±0.70‰)

2.2 Calibration

The experiments were accompanied by a calibration campaign of numerical models seeking to reproduce the stiffness, strength, hysteresis, and cracking behaviour observed. The focus was laid first on fired-clay brick specimens since these structures were deemed to be more vulnerable. Walls were reproduced using a homogenised continuum within a finite-element-method (FEM) modelling approach. The model behaviour was verified against the force-displacement curves and the observed crack fields; Fig. 6 juxtaposes these targets by placing DIC-based crack maps from the tests on the left, the corresponding FE crack localisation in the middle, and the measured versus simulated loops on the right. Different types of walls were investigated for both the one-way as well as the two-way cyclic loading protocols, and the calibration set explicitly included specimens with openings and varying boundary conditions so that both global and local response features were confronted simultaneously (Korswagen et al. 2019).

Walls that had been pre-damaged (by placing a plastic strip on certain masonry joints during construction) were also tested and reproduced. These pre-damaged configurations advanced crack onset and altered early-cycle stiffness, effects that were captured in the models by locally reducing tensile bond capacity along the seeded joints and by respecting the test loading history. Smaller tests on spandrels, where cracking developed mostly vertically due to bending, were also used to aid the calibration; here, micro-modelling with separate

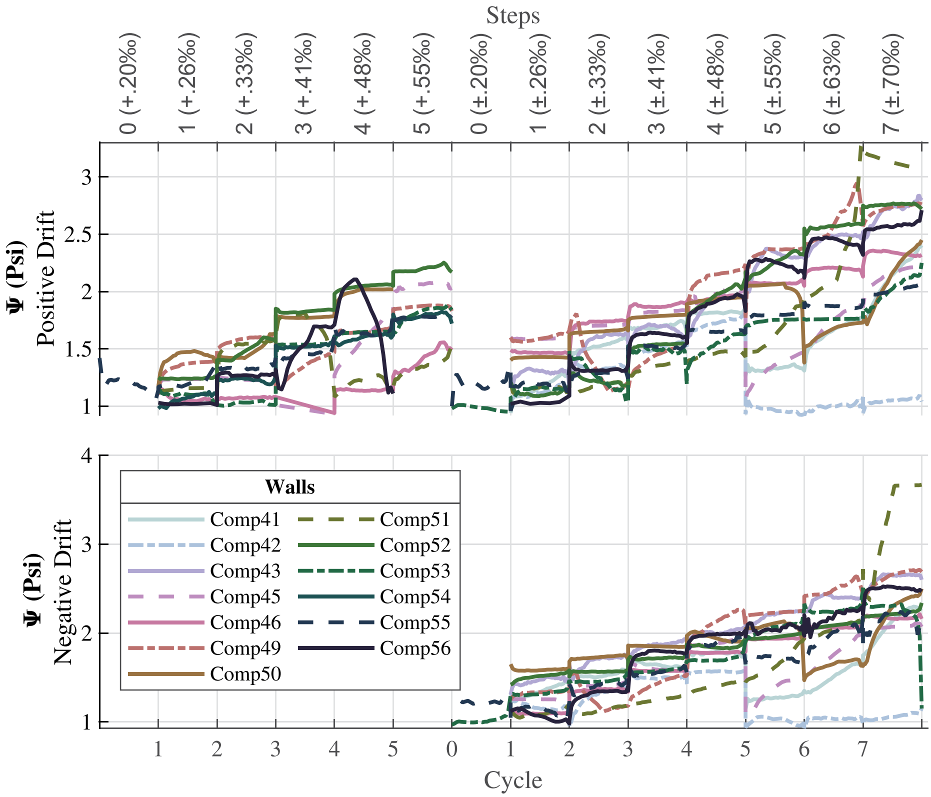

Fig. 5 Damage intensity Ψ progression over cycles and steps during experimental wall tests

brick and mortar phases was employed selectively to resolve single-crack CMOD evolution and to benchmark the macro strategy used for full walls. In all cases, full-field DIC provided not only the visible crack trajectories but also quantitative crack widths and lengths, enabling direct computation of the crack-based scalar damage parameter Ψ that served as a common metric between tests and simulations.

The calibration converged on the Engineering Masonry Model (EMM) as the most effective macro-constitutive law for this scope. The EMM (Schreppers et al. 2016), a smeared, continuum-based model tailored for in-plane URM, captures head-/bed-joint orthotropy, tensile softening with secant unloading, shear friction with cohesion softening, and compression hardening followed by softening, and it allows the user to prescribe the expected diagonal crack orientation: faithful to the staircase cracking typical of these walls (Korswagen et al. 2022). In practice, calibration proceeded iteratively: parameters governing tensile strength and softening were tuned to reproduce first-crack drift and early widening observed by DIC; shear-related parameters were adjusted to match pinching and sliding along toothed cracks; compression parameters were aligned to the peak resistance and the shape of unloading/reloading branches. Throughout, two validation metrics were kept in lockstep: (i) the force–drift loops and (ii) the spatial crack pattern and its evolution, so that matching global response never came at the expense of an unrealistic localisation pattern.

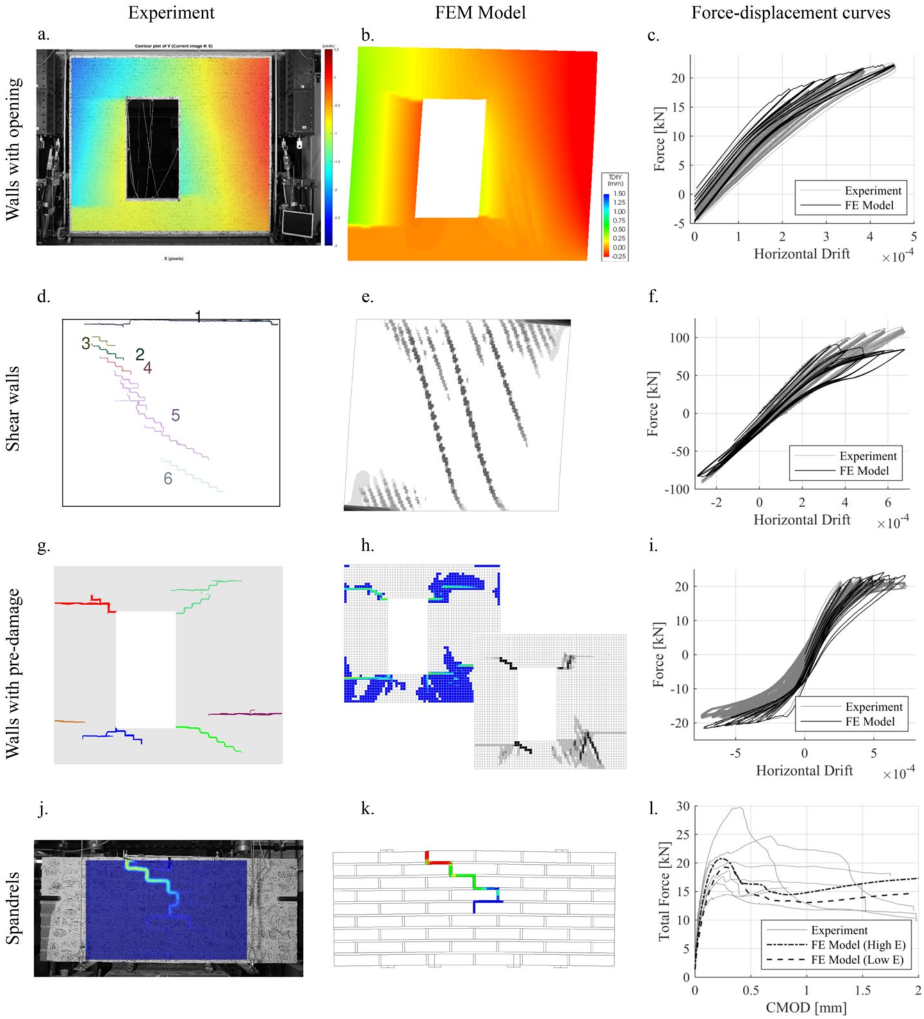

Fig. 6 Calibration overview. Experiments (**a**, **d**, **g**, **j**) are reproduced by finite element models (**b**, **e**, **h**, **k**) in terms of cracking and in force-displacement and hysteresis behaviour (**c**, **f**, **i**, **l**)

One important outcome of this process is that, while the macro models reproduce the trend of damage increase when drift steps up, they under-represent the within-step accumulation seen during many identical repetitions at constant drift. This is consistent with the present EMM not including an explicit cyclic-degradation memory for small-amplitude cycling: in the tests, repeated cycles at fixed drift produced measurable force degradation and incremental widening of a small set of dominant cracks, whereas the calibrated macro models, although correct in the aggregate pattern and global loops, did not degrade as quickly under repetition (Bindiganavile-Ramadas 2018). This acknowledged limitation is precisely what motivates, at methodology level, the surrogate and, ultimately, the Damage Accumulation Function introduced later to account for repetition and uncertainty consistently.

The calibration also leveraged contrasts between materials and configurations. Calcium-silicate specimens showed steeper Ψ growth than fired-clay at equal drift and a greater tendency for unit-splitting, both in walls and in spandrels; the models reproduced these differences by adjusting stiffness, strength, fracture energy and shear-retention parameters within bounds supported by the test data and material characterisation. Boundary conditions (cantilever versus double-clamped) were mirrored from the setups so that anchorage restraint and vertical stress levels were reflected in the shear-to-flexure mix of cracking. For pre-damaged walls, the debonded interfaces triggered earlier localisation and wider cracks at the same drift; model updates confined to the intended joints were sufficient to replicate these shifts without compromising the response elsewhere.

In summary, Figure 6 encapsulates the calibration philosophy: test-measured crack maps and loops on the left/right, FE localisation and loops in the centre/right, and a one-to-one visual and quantitative comparison for each typology considered. Within this framework, the EMM provided a computationally efficient and sufficiently accurate basis to carry experimental trends into modelling: correct initial stiffness and peak resistance, realistic hysteresis in the light-damage regime, and faithful crack localisation across clay and calcium-silicate walls, with the explicit limitation that constitutive cyclic degradation remains to be embedded if one seeks to capture long series of identical repeats. This caveat is carried forward into the surrogate and the DAF, which together supply the sequence-aware, uncertainty-aware layer needed for accumulation analyses.

2.3 Extrapolation

Extrapolation is the process of estimating or predicting values or behaviour beyond the range of known data, based on trends or patterns observed within that data. In engineering or scientific research, it usually involves applying findings from controlled experiments or models to different or broader scenarios, such as larger structures, different loading conditions, or untested configurations. In the context of this paper, extrapolation refers to using the results of laboratory tests and calibrated models to predict how other masonry structures (not physically tested) might behave under similar or more complex seismic loading. In this manner, the calibrated models are adapted and used for NLTH analyses where earthquake acceleration records are applied at the base of the walls.

To maintain fidelity with the experimental insight while moving to dynamic input, the calibrated models from Sect. 2.2 were extended with elements that represent features present in buildings but absent in the wall tests. A line mass was added at the top edge to represent floor inertia and tributary mass from adjacent components; without this, base accelerations would not develop realistic inertial forces in the wall. At the foundation, an interface element was introduced to emulate immediate soil-structure interaction; its stiffness characteristics follow established impedance formulations so that rocking and sliding compliance are represented in a lumped yet mechanically consistent way (Longo et al. 2021; Gazetas 1991). Along the vertical edges, line elements provided out-of-plane bracing and vertical cracking restraint representative of perpendicular (transversal) walls; their axial and rotational stiffness/impedances were tuned within experimentally supported ranges so that the in-plane cracking mechanisms remained realistic for Dutch façades (Prosperi et al. 2025). With these additions, the same constitutive settings (Engineering Masonry Model) and mesh philosophy as in Sect. 2.2 could be carried into the NLTHA domain without re-parametrising the core masonry behaviour (Korswagen et al. 2022).

Dynamic inputs were drawn from Groningen-relevant ground-motion records; groups of representative local records were selected and then scaled to prescribed PGV levels so that amplitude could be varied while preserving the records' frequency content and phasing. The NLTHA monitored global drift, force–displacement response, and the evolution of the crack-based scalar damage parameter Ψ in time; the latter remained the primary link between dynamic response and crack-based light damage, consistent with the experimental and calibration stages. Numerical stability was ensured with the same solution strategy used for the quasi-static calibration, complemented by a time-stepping small enough to resolve the dominant pulses of the short-period Groningen motions, so that peak velocity plateaus and their repetition effects were captured without spurious numerical damping.

The broader literature compiled for this study aligns with these extrapolation choices and informs several implementation details: integrated survey–NDT–FE pipelines for complex masonry and the importance of calibrated dynamics (Chacara et al. 2023); limits of simplified screening versus detailed FE when progressive degradation matters (Ennali 2020); reliability of nonlinear static procedures compared with NLTHA and the preference for capacity-spectrum–type formulations for stiff URM (Giusto et al. 2024), including improved displacement-demand estimators tailored to masonry hysteresis (Guerrini et al. 2021); system-level sensitivities to diaphragm stiffness, connection quality, and multi-storey interaction that condition accumulation paths (Mendes and Lourenço 2015); and NLPO–NLTH comparisons on Dutch URM that motivate using dynamic analyses when sequence effects are of interest (Messali et al. 2022). These strands collectively justify the PGV-driven NLTHA with macro FE and SSI adopted here, as well as the homogeneous/heterogeneous sequence design carried forward and collected in Table 2.

The extrapolations are also characterised by the variations of most parameters, as summarised in Table 2 and Fig. 7. The parameters include: wall geometry (with associated first period T), soil type for the soil-structure interface, a set of properties for the material, an initial damage condition such that the walls are already cracked before conducting the NLTHA, the earthquake records corresponding to four local records (Zeerijp and Westerwijtwerd, near and far (Korswagen et al. 2022), and the PGV sequences. Geometry was varied to reflect common Dutch wall periods; the soil–foundation interface covered stiff and soft

Table 2 Summary of FE model variations, especially homogeneous and heterogenous histories with the extrapolation

Wall geometry	Soil Type	Material Strength	Initial damage	Earthquake event	PGV homogeneous	PGV heterogeneous
		Weak material	Ψ_0=0			
		E=2750 MPa	no damage			
		ft=0.11 MPA				1x16 mm/s + 1x4 mm/s
		Gf=5.6 N/m	Ψ_0=0.5	Zeerijp Near	2 mm/s (2x, 4x, 8x)	1x8 mm/s + 1x16 mm/s
Flexible with window	Sandy clay		invisible damage		4 mm/s (2x, 4x, 8x)	1x16 mm/s + 1x8 mm/s
opening	(stiff)	Standard material	c_w < 0.1 mm	Zeerijp Far	8 mm/s (1x, 2x, 4x)	1x16 mm/s + 1x32 mm/s
T=0.12 s		E=3570 MPa			16 mm/s (1x, 2x, 4x, 8x)	1x32 mm/s + 1x16 mm/s
	Peaty clay	ft=0.16 MPA	Ψ_0=1.0	Westerwijtwerd Near	32 mm/s (1x, 2x, 4x)	2x8 mm/s + 1x16 mm/s
Stiff without opening	(soft)	Gf=11 N/m	barely visible damage		64 mm/s (1x, 2x)	2x16 mm/s + 1x4 mm/s
T=0.07 s			c_w ≈ 0.1 mm	Westerwijtwerd Far	96 mm/s (1x)	2x16 mm/s + 1x8 mm/s
		Strong material			128 mm/s (1x)	2x16 mm/s + 1x32 mm/s
		E=5100 MPa	Ψ_0=1.5			2x32 mm/s + 1x16 mm/s
		ft=0.21 MPA	visible damage			
		Gf=19 N/m	c_w ≈ 0.5 mm			

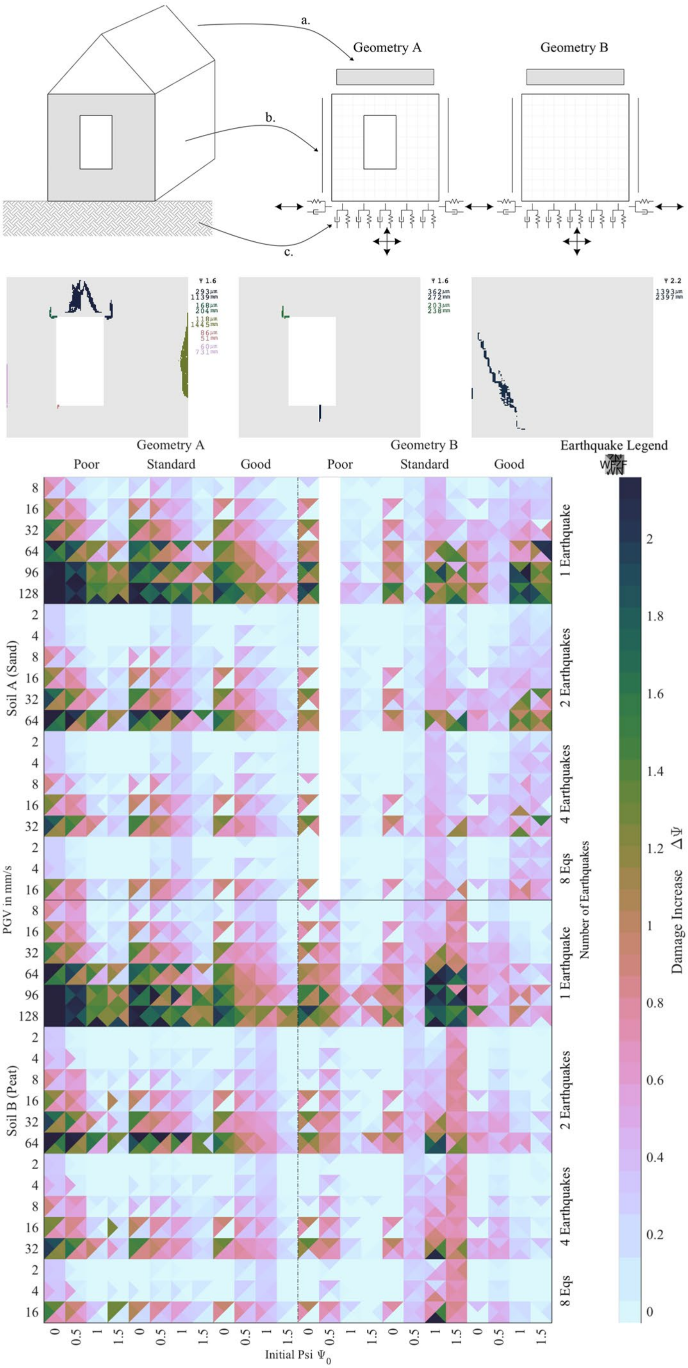

Fig. 7 Extrapolation overview. The wall models are adapted for NLTHA analyses for both types of wall. The damage intensity of the results are interpreted automatically using Ψ. Each square is subdivided into four triangles corresponding to the various earthquake records: ZN, ZF, WN, WF, clockwise from the top

classes; material parameters spanned the experimentally calibrated ranges for fired-clay; and initial conditions included virgin and pre-damaged states consistent with the tests in Sect. 2.2. The PGV permutations are most important and include variations in intensity and number. Two sets are included: a homogeneous sequence, where a model is analysed by a time series composed of a single record, scaled to the same intensity (these results are shown in Fig. 7), and a heterogeneous sequence for which the record is scaled differently. For example, the first combination noted in Table 2 is that of a record scaled to 16 mm/s followed by a record scaled to 4 mm/s. This allows observations regarding the damage effect of events that are smaller or larger than preceding or subsequent events. The results of the heterogeneous sequences are later included in Figure 11.

The coloured triangles in Figure 7 show the intensity of the damage aggravation due to the applied record for all the parameters varied; this allows a comparison of the influence of each parameter. For example, higher PGV intensity leads, predictively, to higher $\Delta\Psi$. Similarly, geometry A shows an overall higher aggravation of damage but is less sensitive to repetition (Number of Earthquakes). The latter is more easily observed in Fig. 8. Here, the relative increase in $\Delta\Psi$ between 1 and 2 or 1 and 4 repetitions is shown in a violin plot. First, one can observe that the higher number of repetitions leads to an overall larger increase in damage. Then, the softer soil B, the stiffer geometry B and the stronger material set, all appear to show a higher sensitivity to repetition than their counterparts.

Because Groningen practice requires decisions under uncertainty, the NLTHA stage also served to characterise variability sources that subsequently appear in the surrogate and DAF layers. Record-to-record variability (for a fixed target PGV), parameter variability (geometry, interface class, material set), and uncertainty in initial condition (pre-damage) each contributed to spread in $\Delta\Psi$. Rather than collapsing this spread into a single nominal curve, the simulation results were retained as distributions at each sequence step; these distributions underlie the PGV-dependent uncertainty term later used by the DAF, with the practical modification that its incremental contribution diminishes with sequence position so that long histories do not accumulate unrealistically broad prediction intervals.

Two notions from Sect. 1 guided the dynamic extrapolation: first, repetition at similar intensity should produce small yet measurable increments in Ψ (crack widening/extension) even when peak drift remains comparable; second, a new event larger than any before should produce a disproportionate “jump” in $\Delta\Psi$. The NLTHA confirmed both trends (Kor-

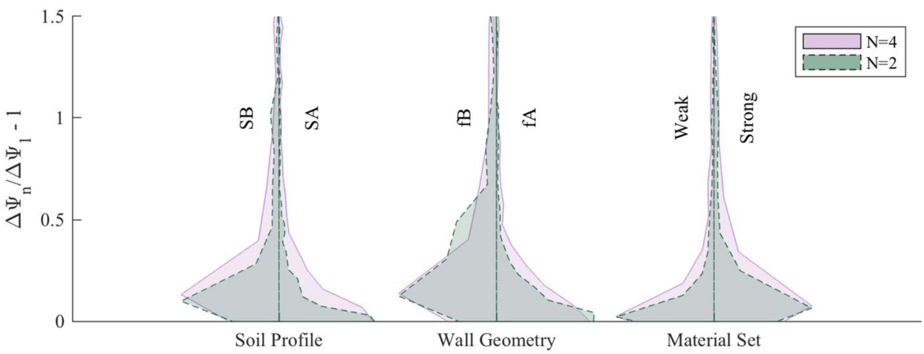

Fig. 8 Comparison of relative damage increase in respect to a single load repletion for three modelparameters against two and four repetitions

swagen et al. 2022). In homogeneous sequences (e.g., repeated 8 mm/s), the first record in the sequence produced the largest increment and subsequent identical records added smaller increases, consistent with the stabilisation seen in the quasi-static repetitions. In heterogeneous series, ordering mattered: a larger PGV following smaller ones produced a more substantial $\Delta\Psi$ than the same large PGV occurring first, and a small PGV following a much larger one produced only marginal additional accumulation, thus reflecting the path dependence expected for crack-localising materials. These observations informed the two-branch structure of the Damage Accumulation Function introduced in Sect. 3 and were used to tune the similarity band that separates "repeat" from "record-breaking" updates.

2.4 Surrogate damage function (Ψ)

A function to estimate the final damage of a model was fitted to the results; this was the focus of Korswagen et al. 2022. Here the damage increase $\Delta\Psi$ was modelled with a function comprising 11 regression coefficients. Moreover, an uncertainty term ε, dependent on the value of PGV was also regressed. Together, damage can be estimated using Eq. 2 next. Other automatic regression models like neural networks or decision trees were also explored but yielded unreliable results. In this manner, the surrogate model is a type of semi-empirical model combining theoretical (mechanics-based) understanding with fitted data (regression).

$$\Psi_F = \Psi_0 + \Delta\Psi\,(\sim) + (V) \tag{2}$$

The surrogate was trained on the dynamic dataset assembled in Sect. 2.3, i.e., the family of NLTH analyses built from the calibrated macro-models, with parameter variations summarised in Table 2. Each simulation delivered, for a single record application, a crack-based increment $\Delta\Psi$ at the end of the motion together with its contributing configuration: geometry (and, by proxy, first period T), façade type (solid wall/wall with opening), material set (fired clay/calcium-silicate), soil–foundation interface class, initial condition (virgin/pre-damaged), and record family, all evaluated at a target PGV. The tilde "~" in Eq. 2 is thus shorthand for this parameter vector. To remain faithful to the experimental scope (light, crack-based damage), responses outside the intended DS1 regime were excluded from fitting, and negative numerical artefacts in $\Delta\Psi$ (rare, due to small oscillations around zero) were clipped at zero to enforce physical non-negativity.

Guided by mechanics and by the calibration insights from Sect. 2.2, the functional form for $\Delta\Psi(\sim)$ was chosen to be low-order and interaction-aware, enforcing basic shape expectations (monotonic non-decreasing with PGV; higher sensitivity for pre-damaged states; soil compliance and opening configurations amplifying increments). Eleven regression coefficients were sufficient to capture these effects across the Table 2 design space, balancing fidelity and interpretability. Fitting targeted the conditional median response to reduce leverage of occasional outliers associated with specific record phasing, while categorical contrasts (e.g., material set, façade type) entered as indicator-based interactions with PGV so that the slope with respect to PGV could differ per typology. Cross-validation was performed by holding out strata in geometry/material/soil combinations and by rotating across record families, ensuring that generalisation was not dominated by a single input dimension.

Because dispersion increases with intensity, the uncertainty term ε(PGV) was modelled as a PGV-dependent, zero-mean, heteroskedastic component. Its variance (and, where useful, tail shape) was regressed on PGV using the residuals left by $\Delta\Psi(\sim)$; this preserves narrow prediction bands at low PGV (where simulations are tightly clustered) and broader bands at higher PGV (where record-to-record variability and parameter interactions naturally widen the spread). The practical safeguard $\Psi \geq 0$ was enforced by truncating the left tail if needed, and fitted intervals were calibrated so that empirical coverage (e.g., 5–95%) matched the distributions observed in the NLTHA ensemble.

Several higher-capacity machine-learning alternatives were tested (e.g., regression trees, boosted ensembles, shallow neural networks), but they proved less reliable for our aims: without explicit constraints they violated basic monotonicity with PGV, were sensitive to extrapolation at the edges of Table 2, and offered limited interpretability for subsequent use in a sequence-aware framework. The semi-empirical regression therefore remained the preferred option: it embeds the mechanics-informed structure (signs and interactions consistent with Sect. 2.2), reproduces the central trend of the NLTHA results with modest parameter count, and exposes ε(PGV) as an explicit object for uncertainty propagation.

There are two main limitations. First, Eq. 2 is event-wise: it predicts Ψ for a single excitation given the parameter vector and therefore does not by itself advance damage through a multi-event history. Second, the fit is anchored to the light-damage regime; outside DS1 (or once localisation mechanisms change), the mapping between PGV and $\Delta\Psi$ may no longer be representative. These limitations motivate the next step of this work: to embed the surrogate inside a sequence-aware update that respects event order and intensity jumps. Indeed, historical PGV series at a site are heterogeneous (cf. Fig. 1), and directly iterating Eq. 2 with $N>1$ would assume homogeneity and independence that do not hold. For this reason, a Damage Accumulation Function is developed in Sect. 3. It distinguishes similar-intensity repetitions from record-breaking events, updates Ψ stepwise through arbitrary PGV histories, and propagates uncertainty in a controlled manner by modulating ε(PGV) across the sequence.

3 Damage accumulation function

From models and experiments, three distinct observations stand out regarding the influence of repeated loading. The loading consists of imposed drift in the experiments and of PGV in the models: 1) A larger load leads to greater damage; 2) repeated loading of similar amplitude leads to a slight increase in damage; and 3) a repeated load, larger than any previous loads, causes a clear increase in damage. In the proposed Damage Accumulation Function, this is captured into a formulation with two parts for $\Delta\Psi$: one for repetitions of similar loads that have previously occurred, and one for loads larger than any previously experienced. The formulation is here next explained stepwise.

In Eq. 2, the final value of Ψ (or Ψ_F) is composed by the initial value Ψ_0, the damage increase $\Delta\Psi$ and an uncertainty term ε dependent on the intensity of the peak ground Velocity (V). The sum of $\Delta\Psi$ and ε should always be equal or greater than zero. $\Delta\Psi$ itself is a function of several parameters such as the material strength, the façade type, the soil type, etc. In Eq. 2 these are denoted with a tilde (~). This can be rewritten simply as Ψ being a function of several variables, where the variables are separated by a vertical bar (|) for clarity:

$$\Psi() = f\left(\Psi_0 \left|V\right| \sim\right) \tag{3}$$

One of the variables that is not evaluated in the surrogate model of (Korswagen et al. 2022) is the number of repetitions of the earthquake "N". While N appears in the formulation, for the subsequent analyses it was assumed to be N=1. For a function that considers damage accumulation due to repetition however, N must be any natural number:

$$\Psi() = f(\Psi_0 \,|V|\, N| \sim) \tag{3.b}$$

Yet, with this formulation, the PGV would adopt a single intensity value, thus forming a homogenous sequence of PGV. Real PGV histories are rarely homogeneous, so a new formulation is required. To account for arbitrary values in realistic sequences of PGV, a function is proposed such that the damage increase for every PGV value in the sequence and the final damage value after the entire sequence can be calculated. The procedure is presented in Figure 9 and is discussed next.

Equation 2 can be rewritten for the damage increase from event i-1 to event i: the value of Ψ following an earlier value of Ψ will be the sum of: the earlier value ($\Psi_{i\text{-}1}$), the instant damage increase ΔΨ, and the uncertainty term ε.

$$\Psi_i = \Psi_{i-1} + \underset{\to i}{\Delta\Psi}\,(\sim) + \frac{\epsilon(V_i)}{i} \tag{4}$$

In this sequence, the following sets can be defined for Ψ and the PGVs (V) linked to each event:

$$V = \{V_1, V_2, V_3, \ldots, V_i, \ldots, V_N\} \tag{5.a}$$

$$\Psi = \{\Psi_1, \Psi_2, \Psi_3, \ldots, \Psi_i, \ldots, \Psi_N\} \tag{5.b}$$

$$V_{\to i} = max\,[V\,(1 \ldots i-1)] \tag{5.c}$$

where: Vi is the PGV at instance or event i and V→i is the largest PGV up until event i, without including Vi, as per equation 5.c.

Within the sets (Eq. 5.a) it is necessary to identify events of similar PGV. The similarity can be assessed by a ratio ρ. The count of all the events with a PGV within the interval 25% smaller or larger than Vi (assuming ρ=0.25), is denoted N_{eq} and is mathematically expressed as:

$$N_{eq} = \sum_{j=1}^{i-1} I_N\,(V_j)$$

$$I_N\,(V_j) = \{\begin{matrix} 1 & if - \rho < \frac{V_j}{V_i} - 1 \leq \rho \\ 0 & otherwise \end{matrix} \tag{6}$$

Thus, ρ is a factor determining the similitude of the earthquakes' intensities. If ρ=0.25 then a PGV that is larger than 25% the maximum PGV occurred until then (V→i) will be consid-

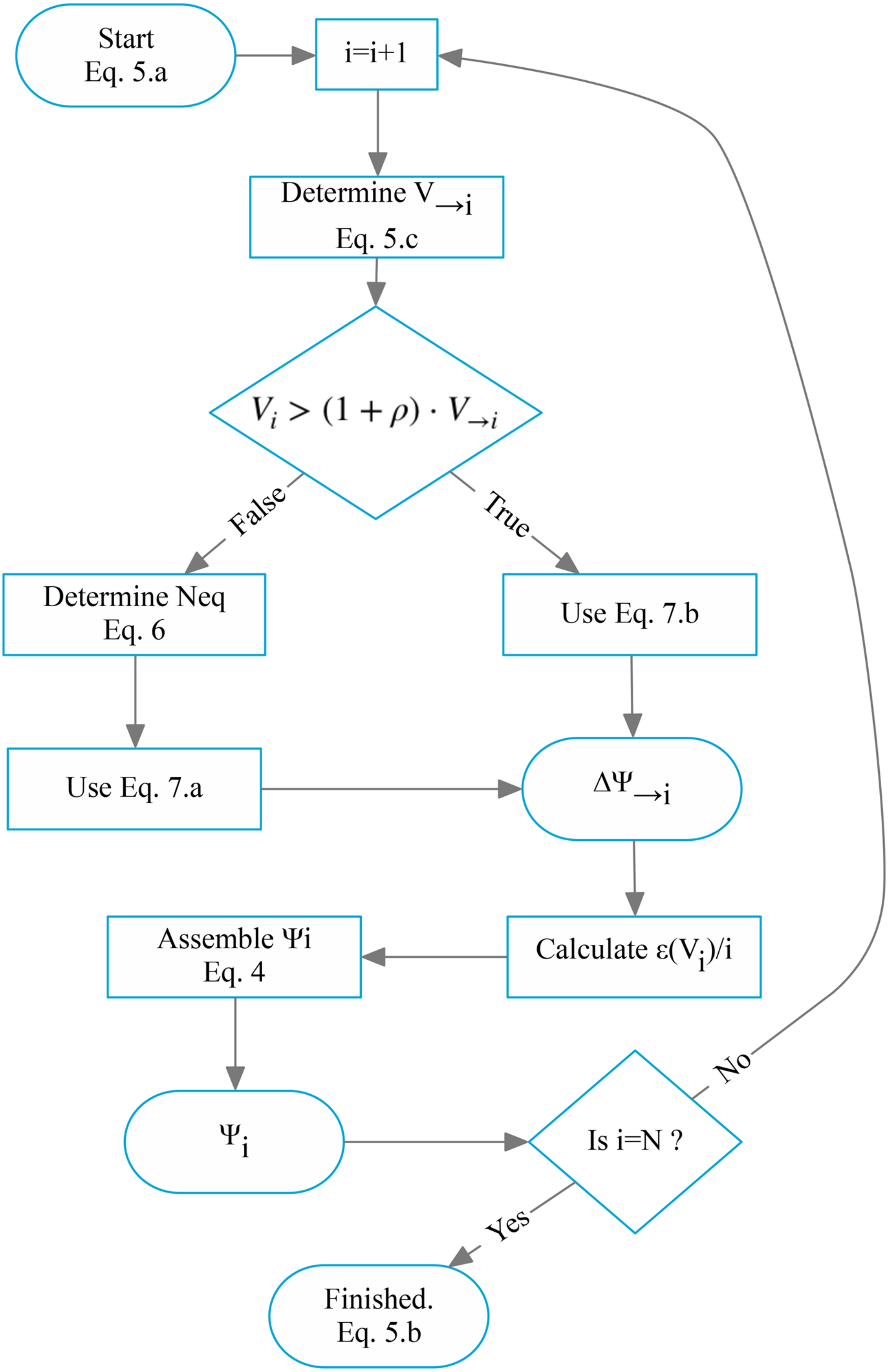

Fig. 9 Flowchart DAF procedure. See Eq. 4 to 8

ered a comparably large event. Hence, for case i, a number of past equivalent events can be computed, or, Vi is identified as large event.

The three distinct observations indicated—that larger load led to greater damage, that repeated loading of similar amplitude led to a slight increase in damage, and that a repeated load, larger than any previous loads, causes a clear increase in damage—are captured into a formulation with two parts for $\Delta\Psi$:

$$\underset{\rightarrow i}{\Delta\Psi} = \{ \begin{array}{ll} \Psi(\Psi_{i-1}\,|V_i|\,N_{eq}+1|\sim) - \Psi(\Psi_{i-1}\,|V_i|\,N_{eq}|\sim) & \text{if } V_i \leqslant (1-\rho)\cdot V_{\rightarrow i}(\text{a}) \\ \Psi(\Psi_{i-1}|V_i\,|2|\sim) - \Psi(\Psi_{i-1}|V_{\rightarrow i}\,|1|\sim) & \text{if } V_i > (1+\rho)\cdot V_{\rightarrow i}(\text{b}) \end{array} \quad (7)$$

Phrased differently: the increase in damage at any instance will depend on whether the PGV is similar (Eq. 7a) or comparably larger (Eq. 7b) than the PGVs of events in the sequence up until that moment. If it is similar, then damage can be computed by evaluating the surrogate function for $\Psi(\sim)$ considering the difference between a homogenous sequence of PGVs with the number of similar events and the same sequence with a number of similar events plus one (N_{eq}+1). This means that $\Delta\Psi$ is indeed the difference in the homogenous sequence for an increase in the number of events by exactly one. If the PGV is much larger than earlier events, then the increase in damage will be the difference between the cumulative damage from a homogeneous sequence that includes this new, larger event and that of a sequence ending at the previous largest PGV. The entire process is schematised in Fig. 9.

When V_i exceeds the prior maximum $V_{\rightarrow i}$ by more than the similarity margin ρ, the structure experiences demand beyond its previous history, causing a disproportionate 'jump' in damage rather than the incremental accumulation seen for similar-intensity repeats. The value of ρ is somewhat arbitrary. What constitutes similar events and when can an event be considered large in comparison to earlier events? From an iterative calibration process considering the results of the next two sections, good agreement was found by setting ρ=0.25.

4 Uncertainty

Equation 4 also contains an uncertainty term. As was determined in (Korswagen et al. 2022), the uncertainty is best characterised as a function of the value of PGV. Small values of PGV carry a smaller uncertainty than larger values. This relationship, a generalised extreme value distribution, is maintained. However, adding this uncertainty at every iteration of $\Delta\Psi$ would lead to an unreasonably large total uncertainty. For this reason, the uncertainty term is weighted by its position in the sequence. The first value would receive the complete uncertainty. For the second value, only half of the new uncertainty is added; for the third, only a third; and so on as per Eqs. 8.4. The last value in the series will receive a relatively small contribution of additional uncertainty. This is reasonable since a large amount of uncertainty has been considered already at that point.

This means also that the influence of a large earthquake will be different if it occurs early or later in the series. Towards the beginning, the uncertainty might receive a larger value while at the end, the value will be smaller. This is also reasonable since the evaluation of the surrogate function also depends on the initial value of Ψ (in this case Ψ_{i-1}). Towards the end of the series, this value will have been affected more by the accumulated uncertainty which will lead to a larger increase without the need of considering the specific uncertainty term corresponding to the large event at the end.

The effect of the uncertainty term can be evaluated with Fig. 10. Here, the results from the FEM models, which were analysed for homogeneous sequences of identical events, are compared against the results from the DAF using the surrogate function (Eq.4) with and without the uncertainty term. For the events of 2, 4, and 8 mm/s, part 7.a of Eq. 7 is used, assuming that relatively small events are more likely to repeat and have similars, while for the sequences of 16 and 32 mm/s part 7.b is used. The median and interquartile ranges of $\Delta\Psi$ compare well for the graphs that include the implemented uncertainty term. In general, the predictions with the DAF appear conservative, yielding slightly larger values of $\Delta\Psi$. This behaviour is preferable to the opposite case. However, the trend and shape of the increase in damage for increasing number of repetitions depicted by the FEM models is maintained with the DAF results. The figure also highlights that for the smaller PGV values, the uncertainty term is more influential in formulating the fitting shape. This is also observed in the relative difference between without and with ε; for the smaller PGVs, this difference is higher.

Moreover, Figure 10 shows that the increase in damage due to increasing PGV is proportional. A twice stronger PGV will lead to twice the damage increase. Similarly, repetitions lead to a larger increase in damage; however, in this case, a repetition only increases damage slightly. Twice the number of repetitions only lead to about 5–15% more damage though this depends on the intensity of the PGV. A larger PGV will have a stronger influence in the amount of damage the repetition will cause. At larger PGVs, the repetition of events leads to larger increases in damage. Note that both the FEM results and DAF predictions in Figure 10 correspond to homogeneous sequences (identical PGV values repeated). The two branches of Eq. 7 (7a for similar-intensity repeats; 7b for record-breaking events) refer to the DAF's internal update logic, not to the input sequence type.

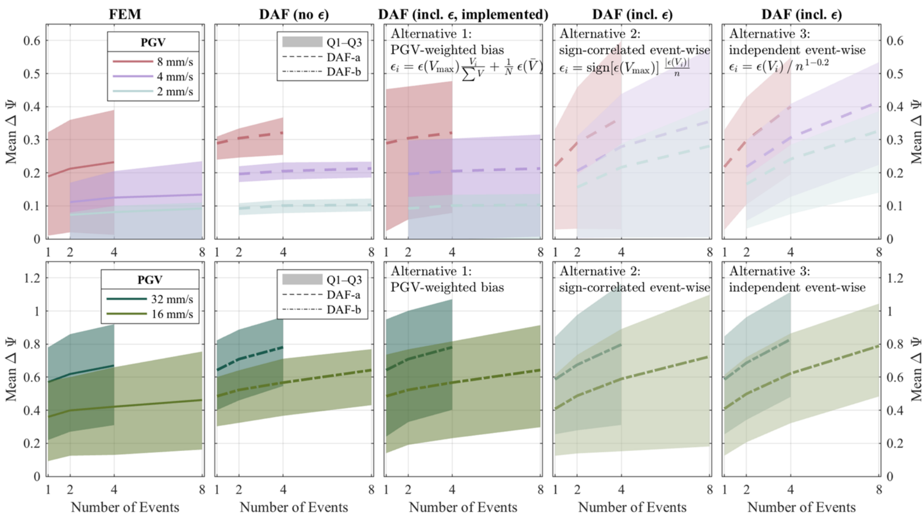

Fig. 10 Comparison DAF formulation with(out) epsilon and FEM results (from (Jafari and Esposito 2016)) for homogeneous PGV sequences. The shaded areas correspond to the interquartile ranges and the centre line is the median

However, Figure 10 also shows various implementations for the uncertainty term. Three are compared. Without the position-based weighting, Alternatives 1 and 3 accumulate uncertainty too rapidly, heavily over-predicting $\Delta\Psi$ for long sequences. The implemented approach (Eq. 8.3 - 8.4, Alternative 2: PGV-weighted bias) applies diminishing weights (1/i) to prevent over-accumulation while preserving appropriate dispersion. The behaviour can be improved if the total uncertainty is considered by a term corresponding to the largest event (which carries the largest PGV-dependent uncertainty) and a smaller term linked to the mean PGV; see Alternative 1, Equations 8.1 -8.2. This leads to a larger predicted initial $\Delta\Psi$ (since it depends on the larger PGV arriving later in the sequence). Alternative 1 is well suited to determine the final $\Delta\Psi$ but is less capable of accurately showing the intermediate Ψ_i. For this, Alternative 2 is preferred.

Alternative 1:

$$\epsilon_{Total} = \epsilon\left(V_{max}\right) + \epsilon\left(V_{Mean}\right) \tag{8.1}$$

$$\epsilon_i = \frac{V_i}{\sum_{j=1}^{N} V_j}\epsilon\left(V_{max}\right) + \frac{1}{N}\epsilon\left(V_{Mean}\right) \tag{8.2}$$

Alternative 2:

$$\epsilon_i = s\frac{|\epsilon(V_i)|}{i}, s = sgn\left(\epsilon(V_{max})\right) \tag{8.3}$$

$$\epsilon_{\text{Total}} = \sum_{i=1}^{N} \frac{\epsilon\left(V_i\right)}{i} = \frac{\epsilon\left(V_1\right)}{1} + \frac{\epsilon\left(V_2\right)}{2} + \frac{\epsilon\left(V_3\right)}{3} + \ldots + \frac{\epsilon\left(V_N\right)}{N} \tag{8.4}$$

Alternative 3:

$$\epsilon_{\text{Total}} = \sum_{i=1}^{N} \frac{\epsilon(V_i)}{i^{0.8}} \tag{8.5}$$

$$\epsilon_i = \frac{\epsilon(V_i)}{i^{0.8}} \tag{8.6}$$

Similarly, the heterogeneous sequences are compared between FEM results and DAF predictions in Fig. 11. Here, the difference between one event of 8 mm/s followed by another of 16 mm/s (1×8+1×16) and two events of 16 mm/s (2×16) can be observed, for example. The figure has been put together such that the (homogeneous) FEM results for intermediate steps for a particular sequence are available. In this manner, the effect of having a large event following smaller events, or multiple smaller events, can be assessed.

The shape of the distributions of $\Delta\Psi$ for FEM and DAF is quite similar. Sometimes, the mean $\Delta\Psi$ of the FEM models is higher than the mean produced by the DAF, but the distributions for the DAF results extend a bit higher. This is because the FEM results seem skewed, with a mean close to the upper 75% quantile, which is probably the result of the limited

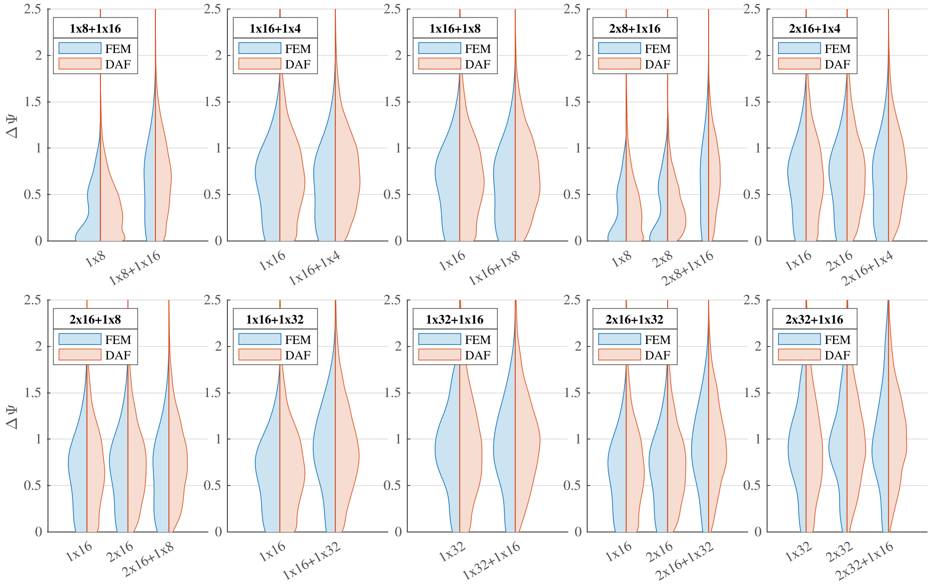

Fig. 11 Comparison DAF and FEM models for heterogenous sequences, increase in damage as ΔΨ. These 'violin' plots show the distribution among the model results (FEM) or simulations (DAF)

number of models and the specific parameters chosen for these. Moreover, the DAF has a much larger number of simulations which allows the extreme-value-distributed uncertainty parameter to generate some few results with a larger ΔΨ. The graph also shows for example, that indeed, 1×16 outputs a smaller damage increase than $1\times16+1\times4$—the distribution shifts slightly up. Figure 11 confirms that the DAF reproduces key trends: repeated events increase damage (compare 1×16 to 2×16), higher PGV yields larger ΔΨ, and sequence order affects final damage only marginally (compare $16+32$ to $32+16$).

This figure emphasises the key observations from the FE models and which are reproduced in the DAF:

- Rrepeated earthquakes lead to additional damage,
- The higher the PGV, the larger the damage increase,
- In a history or sequence with low PGV values, a relatively large value leads to a stark increase,
- In a history with similar PGV values, an additional event leads only to a small increase,
- The final values of damage between a large and a small, and a small and a large PGV values are similar (see $32+16$ and $16+32$).

Finally, a comparison can be drawn against the repetition behaviour observed in the experiments, as per Fig. 12. However, validating the DAF through experimental results is challenging and thus this comparison is done only qualitatively or phenomenologically for several reasons:

Firstly, the experiments focused on repeating displacements, whereas the DAF is implicitly evaluating repeated force applications. The earthquake-induced vibrations applied to

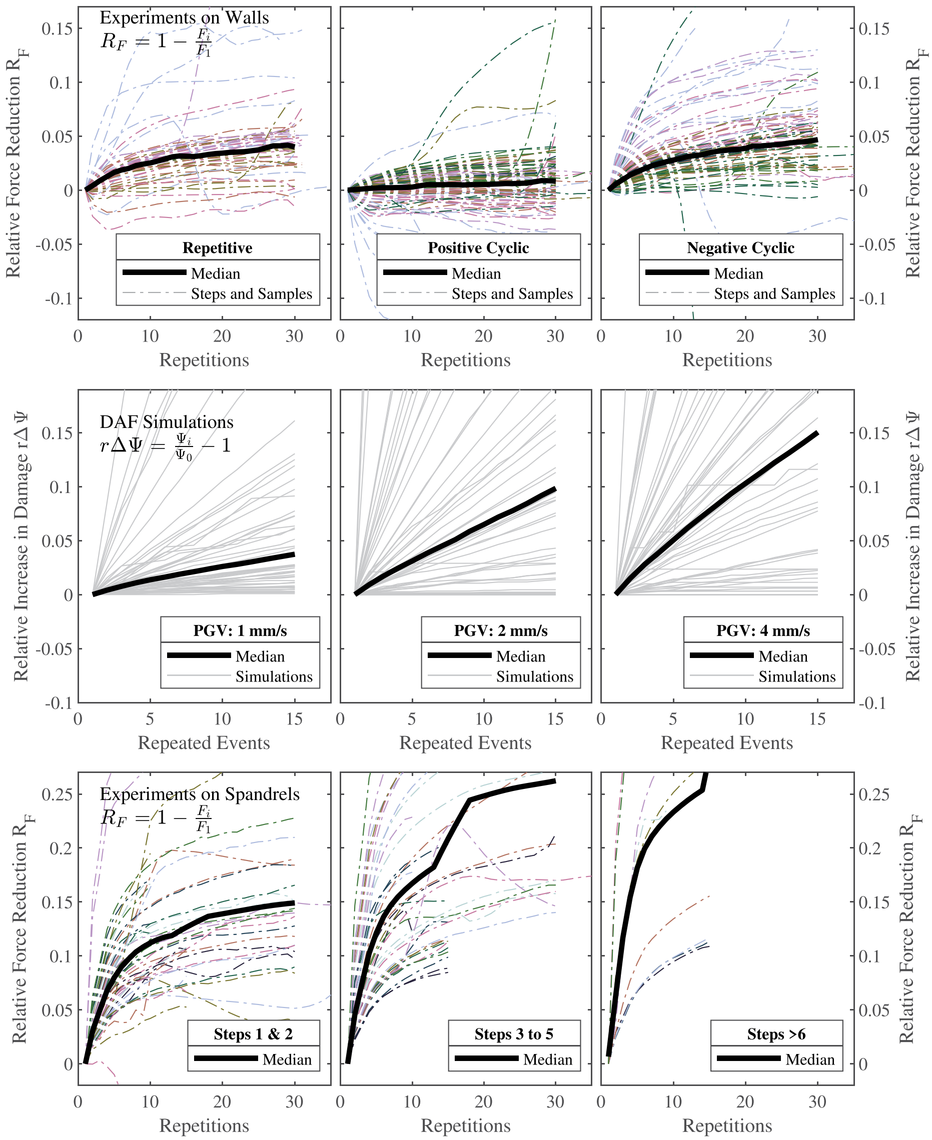

Fig. 12 Comparison against experimental results for Ψ and force degradation. Qualitative comparison of experimental repetitive force reduction in walls (top) and spandrels (bottom) against DAF's progressive increase in damage (middle). Experimental steps 1–2 (low drift) correspond qualitatively to DAF results at PGV ≈1 mm/s; steps 3–5 (intermediate drift) to PGV ≈2 mm/s; steps > 6 (higher drift) to PGV ≈4 mm/s. The one-way repetitive, positive cyclic, and negative cyclic phases reflect increasing cumulative demand, analogous to increasing PGV in the DAF

structures generate accelerations that translate into inertial forces. Similar events with comparable frequency content will induce similar forces, assuming structural damage progression does not significantly alter the dynamic response—an effect already accounted for in FEM models.

Secondly, experimental procedures included extensive repetitions, typically applying thirty repetitions per step to observe stabilisation in force reduction, totalling approximately three hundred repetitions. Thirty repetitions alone already represent numerous repeated earthquake events, and this large number aimed to replicate the effect of multiple effective vibration cycles. This substantial repetition volume, however, complicates direct comparisons.

A third consideration arises because the DAF is primarily formulated to assess heterogeneous sequences; this effect was limited in experiments. Specifically, the repetitive protocol involved five one-way cyclic steps, while the cyclic protocol featured seven two-way cyclic steps. Minimal force reduction occurred in the first five cyclic steps, analogous to minimal damage increases from events with PGVs smaller than previously experienced. Notable force reduction appeared in the final two steps, reflecting significant damage increases from larger PGV events despite previous events.

Thus, comparing experimental observations of repeated displacement events to force-based repetitions in the DAF requires assuming that the damage increase from repeated force events corresponds to the force reduction observed in displacement repetitions—which is not a direct comparison. Nonetheless, the force reduction, normalised relative to initial force at each step, can be compared to the damage increase observed by the DAF: the experimental behaviour and DAF predictions exhibit similar decreasing slopes with increasing repetitions.

Experiments on spandrels—where damage was constant due to crack-mouth width control—provide a more direct comparison. Still, spandrels represent smaller masonry components focusing on single cracks, differing from the DAF's broader scope intended for larger masonry elements with multiple cracks. As illustrated in the bottom row of Fig. 12, spandrels are categorised by the steps of the loading protocol. This categorisation aligns with increasing PGVs used in DAF plots. Consequently, larger steps or PGVs correspond to greater force reduction and damage increases in the DAF results.

5 DAF Discussion

The formulation of the DAF rests first on experimental evidence for light, crack-based damage and for repetition effects. Full-scale wall and spandrel campaigns with high-resolution DIC established that cracks widen and extend even under constant drift repetitions and that force/stiffness degrade direction-dependently after one-way cycling; they also defined the crack-based scalar Ψ used here as the carried damage state. Material characterisation and multi-scale testing for Dutch URM types (fired clay; calcium-silicate) underpin the parameter ranges used in our surrogate and confirm mechanism differences (joint-following vs unit-splitting) that explain steeper Ψ growth for calcium-silicate at equal drift (Jafari and Esposito 2016; Messali et al. 2018; Esposito et al. 2019; Grottoli et al. 2019). Independent work connecting crack patterns to residual stiffness/strength and diagnostic protocols supports the idea that a crack-centric state is a natural metric for damage progression at DS1 (de Vent 2011; Latifi et al. 2023; Dolatshahi and Beyer 2022).

Second, the DAF's sequence awareness, separating "similar-intensity repeats" from "record-breaking events", reflects Groningen-focused modelling and assessment studies where repeated, small motions accumulate visible damage, but a new maximum causes a disproportionate jump. Portfolio workflows combining induced-seismic hazard, fragility and consequence analysis frame the regional risk but are largely memoryless, motivating a state-updating rule (van Elk et al. 2019; Crowley et al. 2017, 2019). Nonlinear FE explorations explicitly looking at repeated events in Groningen illustrate both “nudge” and “jump” behaviours that our two-branch update formalises (Sarhosis et al. 2019; Grant et al. 2019). The choice of PGV as the intensity driver and the construction of realistic event sequences are aligned with Groningen-specific and short-distance GMPE/GMPM work and with regional magnitude bounds used for scenario exploration (Bommer et al. 2017; Atkinson 2015; Suzuki and Iervolino 2017; Zöller and Holschneider 2016). The practical 2 mm/s context for visibility/claims is consistent with Dutch administrative practice and local histories with many exceedances (wetten.overheid.nl, 2023).

Third, the surrogate $\Delta\Psi(\cdot)$ embedded in the DAF is calibrated against NLTHA built from macro-models validated on the same DIC evidence so the mapping from intensity and parameters to crack increment is consistent with the experiments. The macro-modelling strategy (Engineering Masonry Model with orthotropy, tensile softening with secant unloading, shear friction/cohesion softening, and compression hardening/softening) follows established validation/benchmark efforts and target behaviours for Dutch URM (Schreppers et al. 2016; Bindiganavile-Ramadas 2018; D’Altri et al. 2020). Building context for dynamics (tributary mass, transversal restraint) and near-foundation SSI are included following Groningen-tailored SSI developments and classical impedance formulations, which our models inherit (Longo et al. 2021; Gazetas 1991). The event-wise surrogate and its role in DAF are presented in detail in the crack-based fragility study for light damage (Korswagen et al. 2022).

Fourth, the uncertainty scheme in the DAF (PGV-dependent dispersion with diminishing incremental weight along the sequence) comes from how variability appeared in the NLTHA ensemble: low spread at small PGV, wider spread at larger PGV, plus contributions from geometry, material set, SSI class, record family and initial condition (virgin/pre-damaged). Rather than over-accumulating variance across long histories, the weighting preserves realism while still recognising that higher-intensity events are more uncertain. This sits alongside established, event-centric uncertainty treatments in masonry fragility/EMS frameworks, which the DAF complements by carrying state between events (Lagomarsino et al. 2013; Crowley et al. 2019; Grünthal et al. 1998; Lovon et al. 2018).

Fifth, the multi-hazard context is informed by settlement-induced façade damage research and Groningen socio-economic studies. Progressive cracking under angular distortion provides a clear analogue for accumulation and for the interaction between long-term actions and repeated light earthquakes (Burland and Wroth 1974; Prosperi et al. 2023, 2025). The societal backdrop underscores why an explicitly cumulative model matters for decision-making and policy, both in the years leading up to and in the policy choices culminating in the gas field’s closure [Boelhouwer et al. 2018; van der Voort et al. 2015; Mulder et al.2018; Reuters, 2024].

Finally, the DAF is designed to be compatible with, not a replacement for, existing practice. It uses the same intensity measures and typologies as regional fragility models (Crowley et al. 2017, 2019), the same modelling backbone acknowledged in URM reviews and validation reports (Schreppers et al. 2016; D’Altri et al. 2020), and it connects to building- and component-scale test evidence across Dutch masonry (Jafari and Esposito 2016; Messali et al. 2018; Esposito et al. 2019; Grottoli et al. 2019). Analogies from infilled-frame modelling further reinforce the generality of sequence effects in built masonry systems (Filippou et al. 2019). In short, Sect. 3's two-branch, sequence-aware update of Ψ encompasses observed Groningen behaviours, is calibrated on existing models, respects established uncertainty structure and remains interpretable within the standard European masonry damage scales.

6 Applications

The purpose of introducing the DAF is not merely methodological; it is to enable history-aware assessments wherever sequences of small, induced events may accumulate light, crack-based damage in masonry. The examples in this section therefore serve as demonstrations of capability, they show how the DAF is used, what kinds of outputs it produces, and which insights it can unlock rather than as definitive site-specific predictions. These examples are paramount to the proposal of the DAF.

The numerical values shown are contingent on the chosen parameters (typology, soil-interface, geometry, material sets, initial condition), the PGV histories or scenarios adopted, and the modelling/calibration envelope established earlier for DS1 and in-plane wall/portal behaviour. As such, the figures and maps should be read as illustrations of the workflow and its sensitivity, not as conclusive statements about any particular location or building.

We organise the applications with three complementary aims. First (Sect. 4.1), we apply the DAF to historical PGV sequences at specific sites to demonstrate sequence-aware updating of Ψ and to make clear why order and repetition matter: small, repeated events cause modest increments, while a new maximum produces a pronounced jump. Second (regional mapping in Sect. 4.1), we show how the same machinery extends to gridded analyses, yielding spatial contours of exceedance probabilities under history-aware accumulation; these maps clarify patterns but remain conditional on the input distributions (e.g., GMPE-based PGV sampling, independence assumptions between grid cells). Third (Sect. 4.2 and 4.3), we illustrate decision-facing uses: the concept of damage hastening, which quantifies how repeated vibrations advance the timing of light-damage realisation relative to other time-dependent processes, and scenario exploration in which alternative seismicity futures translate into different trajectories of damage exceedance over time. Throughout, we juxtapose DAF-based results with quicker, event-wise baselines to emphasise when and why a sequence-aware model changes the history of damage aggravation.

Two framing points guide the interpretation. (i) The applications adopt PGV as the intensity driver, consistent with induced-seismic motions, Dutch practice, and the calibration domain; this choice ties also to drift and to the crack-based parameter Ψ. (ii) The analyses respect uncertainty: dispersion is carried explicitly via the DAF's PGV-dependent term and via parameter sampling. Consequently, the methodological insight, that history matters, and that repetition and new maxima play different roles, should be taken as the main takeaway. For operational decisions at a specific site or portfolio, the DAF should be re-run with site- and typology-specific inputs and with checks for system-level effects beyond the single wall proxy used here.

6.1 Sequence of vibrations

The earthquake sequence of Fig. 1, corresponding to the earthquake intensities computed using Ground Motion Prediction Equations (GMPEs) for the town of Loppersum over the last decades, will result in an accumulation of damage for masonry buildings. Assuming that no other hazards or interventions have taken place in this timeframe, the DAF can be directly employed to calculate the cracking damage progression. The results are presented in Figure 13 and discussed next.

Four different initial damage levels are investigated for before the first event: no initial damage ($\Psi_0=0$), invisible cracking ($\Psi_0=0.5$), just-visible cracks ($\Psi_0=1$), and clearly-visible cracking damage ($\Psi_0=1.5$). The figure includes the expected value of Ψ and the band for the prediction interval within 5–95% generated not only due to the uncertainty term but also to variations in soil, material strength, wall geometry, as per Fig. 7 and the framework of (Korswagen et al. 2022). One can observe that the second event, which reached a PGV of 8 mm/s (this is the value that would only be exceeded with a probability of 25% according to the GMPEs), is the first to noticeably increase damage. Subsequent events only increase damage slightly until the tenth event (Westeremden of 2006) which produced a PGV of 16 mm/s. At this point, a masonry building that started without damage ($\Psi_0=0$), would show visible cracks ($\Psi\geq1$) with a probability of at least 5%. The next event to contribute significantly to damage accumulation is that of Loppersum in 2008, which due to its epicentre, being close to the town, generated relatively large PGVs. In comparison, the event of Huizinge of 2012 with a Mw = 3.6 (Zöller and Holschneider 2016), led to lower PGVs and lower

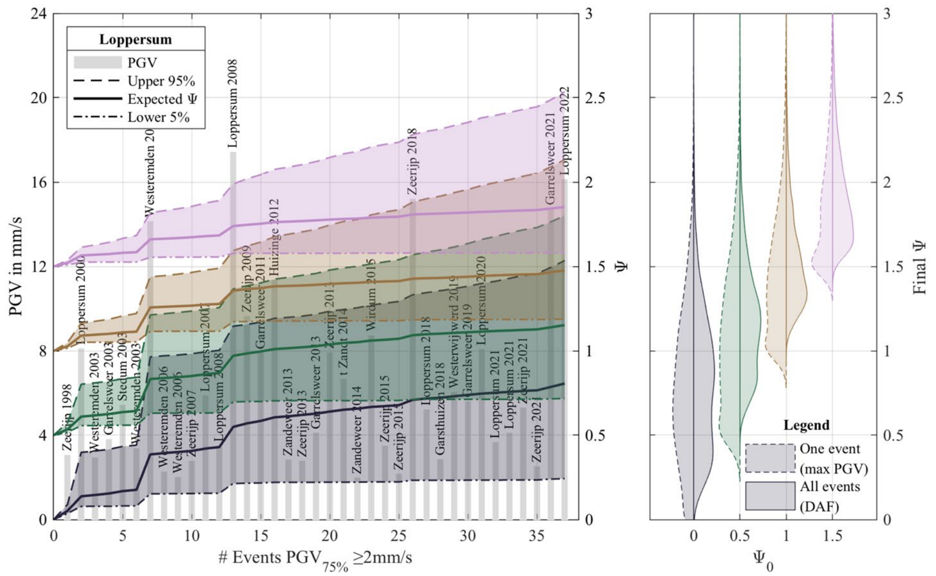

Fig. 13 DAF for Loppersum. Sequence of earthquake events and their PGV at the town of Loppersum (left axis). On the right axis, the increase in damage, measured with Ψ is given for four distinct starting conditions from $\Psi_0=0$ to $\Psi_0=1.5$. The confidence margin for Ψ, in the interval 5% to 95%, shows the probability of damage. On the right graph, the distribution shape is shown for the state at the end of the earthquake sequence, for both the DAF approach (right) and one considering only the maximum PGV in the history

damage accumulation since its associated PGV is smaller than that of the preceding events mentioned. Ultimately, at the end of the observed period, also depicted in the right "violin plot" of Fig. 13, the probability of Ψ exceeding visible damage is about 30% for a case that started with no damage, and more than 70% for a case that had some invisible damage. The probability of exceeding light damage ($\Psi \geq 3$) is too small (<1%) for this simulation and not represented in Fig. 13. The violin plot also presents the distribution of damage probability for the situation with only one event, whichever generated the largest PGV for the sampled case. This serves to assess the DAF and illustrate the effect of considering the accumulation of damage. One can observe that the DAF results produce larger damage increases, with the distributions shifting upwards.

The simulation can be extended to a regional grid, so that, for every cell in the grid, the history of PGV and its associated damage progression is determined as in the example of Fig. 13. Then, at the end of the observed period, the distribution of damage for the various initial damage conditions can be summarised by formulating iso-probability lines. These form the contours presented in Fig. 14. At the top of the figure, the epicentres and magnitude of the events are located in a map coupled to a timeline of the events. Three iso-probability set of contours are highlighted and linked to a probability of damage given an initial condition as indicated at the top right of each map. The probabilities included range from 1 in 2 (50%) to 1 in 10 000 (0.01%). At the centre of the region, where the seismic events were strongest and most epicentres took place, the probabilities of accumulated damage are also the largest. Indeed, at the centre of the region, the probability of visible damage ($\Psi \geq 1$) is larger than 50% while, for most of the 6 km buffer zone of the gas field and including a large area outside of it, it is larger than 0.1%. The probability of exceeding Damage State 1 (DS1, $\Psi \geq 2.5$) is limited to about 1% in the very centre of the region, though this area extends significantly if the initial conditions of the masonry structure already displayed visible cracks ($\Psi_0 = 1$).

Note that there is an important distinction between the method applied in Figs. 13 and 14. For the earlier figure, damage has been determined for the specified PGV sequence which corresponds to the PGV value associated with the 75% percentile value determined with the GMPEs. For the iso-probability lines of Fig. 14, however, the uncertainty in PGV prediction is considered as per the formulation of Bommer (Bommer et al. 2017). For each grid cell, about $100 \times 100\,\mathrm{m}^2$, the simulation samples the PGV randomly for each event generating about two hundred different timelines per grid cell; for simplicity, the timelines are not correlated between neighbouring grid cells. Then, for each timeline, the DAF is applied to a large sample of walls (buildings). In this manner, the simulation for the entire region is about 20 billion unique samples. Note that the number of buildings, soil and material parameters are identical for each grid cell. Simulations with the existing building stock have not been conducted. The Montecarlo simulation follows the same distributions employed in the earlier section and in (Korswagen et al. 2022). For simplicity, uniform distributions were assumed for wall typology, soil class, and material properties across all grid cells; the actual building stock was not modelled.

The maps and contour lines presented in Figure 14 are specific to fired-clay masonry structures. Yet they provide the probability of exceeding particular crack-based damage conditions considering the accumulation of damage over the bulk of the seismically-active period observed. This is an important contribution that differs from traditional methods that

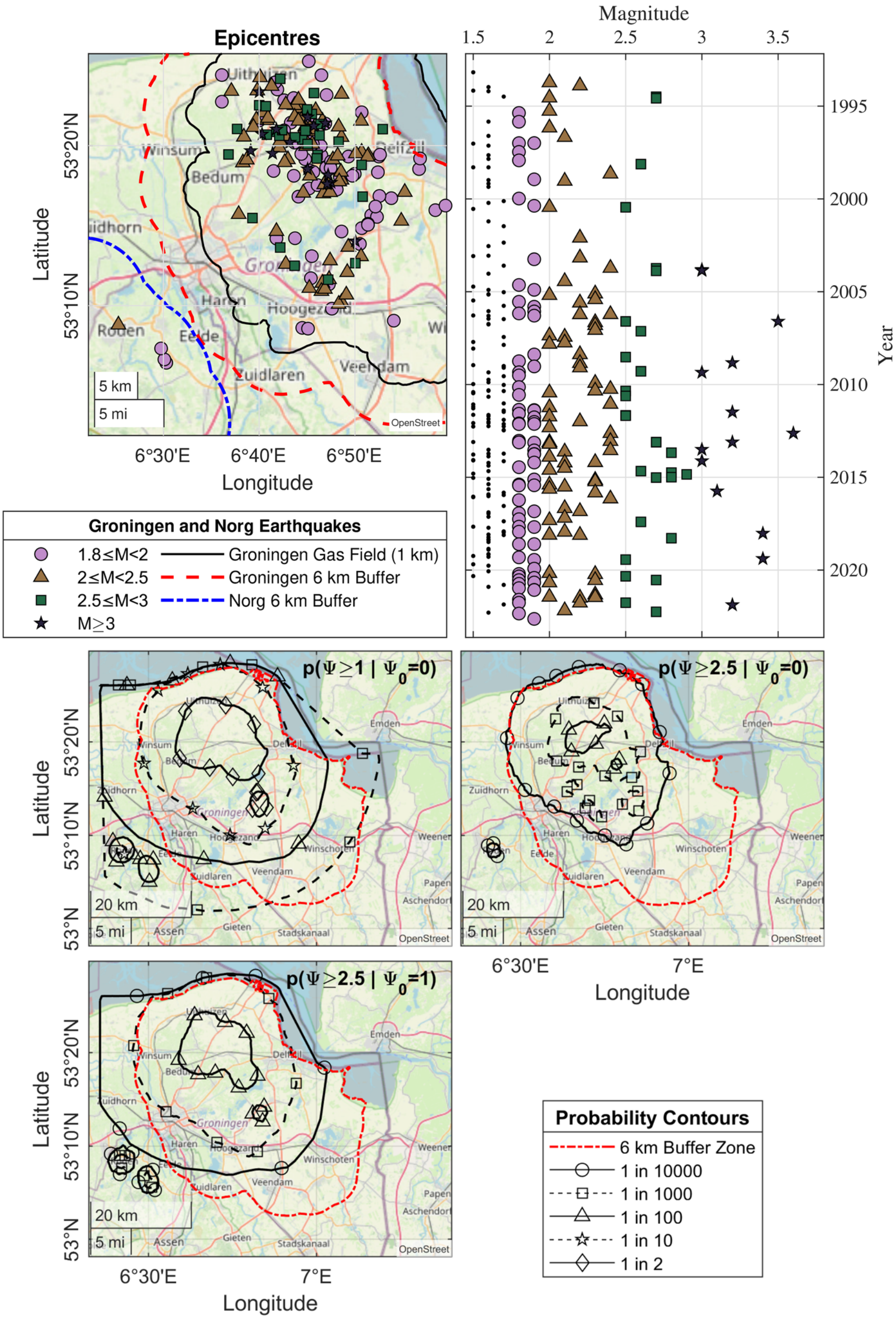

Fig. 14 DAF for Groningen region. Top, epicentre of past earthquake events, magnitude and distribution in time. Bottom, maps with contours of probability of damage from accumulated damage over the indicated time period

typically assess the probability of damage given a single PGV value or a distribution of the maximum PGV in combination with fragility curves.

Consequently, to assess the proposed DAF method, four different calculations were conducted:

- 1) DAF with a probabilistic distribution of PGV as described in the previous paragraphs;
- 2) DAF with PGV sequences formed from the 99th percentile PGV;
- 3) Fragility curves convoluted and integrated with the distribution of PGV corresponding to the event with the largest PGV; and,
- 4) Fragility curves in combination with the maximum of the 99th percentile PGV.

The methods have been listed in order of slowest (most resource intensive) to quickest.

In brief: method (1) applies DAF to probabilistically sampled PGV sequences and is the most complete but slowest approach; (2) uses a deterministic 99th-percentile PGV in DAF, providing the most conservative single estimate; (3) evaluates fragility curves—derived from the NLTHA-calibrated surrogate (Sect. 3) at the single-event level—at PGV values sampled from the distribution of the largest event in the sequence, thus ignoring accumulation; (4) evaluates the same single-event fragility curves at the deterministic maximum PGV only. Methods (3) and (4) omit sequence effects entirely and serve as benchmarks against which the DAF-based methods (1) and (2) can be compared.

All four methods provide final probabilities of damage in the same order of magnitude. However (2) is the most conservative, leading to the highest predictions, followed by (4). These two yield iso-probability areas about twice as large as (1) and (3), yet (4) is extremely quick to run, closely followed by (3). In this sense, evaluating (2) and (4) can be disregarded in favour of (3), for a quick assessment, and (1) for the most accurate assessment. The fragility curves (3) produce higher probabilities of damage towards the centre of the region in comparison to (1), while leading to lower probabilities towards the edges of the gas field. This can be explained because of damage accumulation. For a single event, the undamaged structure will become more damaged, while for a sequence of events, the earlier, smaller events have contributed to some small damage to the structure, which alters its response to the later larger events. At the edges of the region, the effect of multiple small events leads to more damage than that of a single event far away.

In this light, we can assume that the results with the DAF (1) are truer to reality than (3) since they consider the accumulation from multiple events. However, without empirical validation data, which is not available, it is not possible to verify this assumption.

6.2 Damage hastening

The concept of 'damage hastening' refers not to the aggravation of existing damage, but to the earlier occurrence of damage that would otherwise have appeared later in a structure's life. Figure 15 serves to illustrate this definition. In this graph, two situations are compared. Consider a building, which, due to material ageing, lack of maintenance, other autogenous causes, or an expected damaging hazard, will develop damage over time; in the figure, settlement is described as the expected source of progressive damage. Due to a second hazard, however, damage will accumulate more quickly. The DAF is used to assess the accumulation of damage because of vibrations. In this example, the damage aggravation in

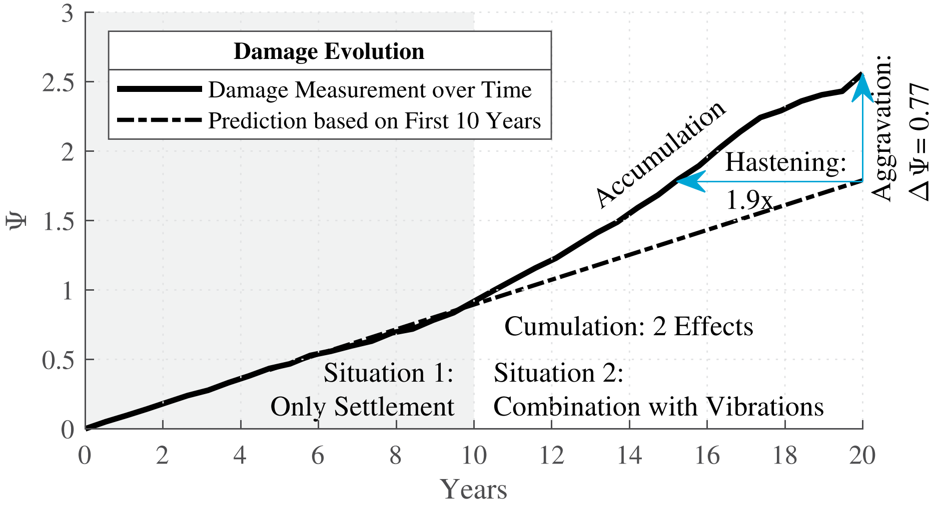

Fig. 15 Example of damage hastening. The concept of damage hastening is explained with this diagram: a damage level that would have occurred later in the life of a structure occurs earlier because of the contribution of a hastening hazard

the second period develops in almost half the time: this is hastening of this damage and can be quantified by determining how much more quickly expected damage is realised due to the influence of a second hazard. In this manner, this metric can be used to better describe the impact of induced seismicity in a region where it was not relevant before. Four terms are thus defined in the figure with subtle differences:

- Cumulation: the combination of various hazards or damaging actions.
- Accumulation: the progressive increase of damage due to repeated actions or the passage of time.
- Aggravation: the damage increase ($\Delta\Psi$) due to a particular cause at a given moment in time.
- Hastening: the earlier occurrence of a given damage increase due to effects of a secondary hazard.

6.3 Simulation of potential future scenarios

In the context of damage hastening, the role of time is critical. While time itself is not inherently a hazard, in specific multi-hazard scenarios, the progression of damage is intrinsically linked to the passage of time. Thus, it becomes practical to represent time on the hazard axis rather than, for example, PGV or soil angular distortion.

To limit the effect of seismicity on existing (masonry) structures, the Dutch government evaluated various scenarios of reduced gas extraction aimed at lessening seismic events. We consider three hypothetical gas production scenarios, each influencing the annual occurrence and magnitude of seismic events differently. Although the exact physical relationship between gas extraction dynamics and seismicity is complex and beyond the scope of this paper, we rely on reasonable assumptions to define the mean annual event rates for these scenarios (summarised in Table 3). These assumptions are derived from historical seismic data, specifically focusing on events exceeding a magnitude of 1.5. Table 3 presents the three scenarios, differentiated by their respective mean annual seismic event rates. For illustrative simplicity, the distribution of magnitudes within these scenarios mirrors historical patterns, and the spatial distribution of epicentres remains consistent with past data, including a magnitude correlation. While the realism of these assumptions warrants further investigation, this simplified approach effectively facilitates scenario comparison. Each scenario projects a distinct evolution of seismicity, affecting the frequency and magnitude of future seismic events. Consequently, each scenario translates into a different anticipated progression of structural damage over time. The DAF provides an ideal framework for addressing these scenario-based analyses.

Figure 16 illustrates the Weibull distribution fitted to historical event magnitudes, highlighting the frequency of seismic events greater than magnitude 1.5 over the period 1990–2024. The historical trend indicates an average annual rate of approximately 11.5 events. Using these historical data, projections of future annual event rates under the three scenarios were derived. The spatial distribution of seismic events is also detailed in Fig. 16. Beta distributions fitted separately to the latitude and longitude coordinates of historical epicentres provide the basis for simulating spatial patterns. Adjustments based on magnitude clustering, especially prominent for larger events, can be applied as needed. Again, this is a statistical approach to simulating future events and is not based on a physical understanding of seismicity; it is used herein to demonstrate the application of the DAF for damage prediction and evaluation of scenarios.

The scenario simulations sample event occurrence daily using Poisson arrivals at the scenario-specific annual rate, with magnitudes drawn from the fitted Weibull distribution and epicentres from the fitted Beta distributions.

Simulations for each scenario generate multiple probabilistic timelines of seismic events. The pool of timelines for each scenario has a mean yearly rate linked to the individual scenarios. Each simulated timeline involves daily sampling to determine the occurrence of events, including their magnitude and epicentre. Hundreds of simulations per scenario yield probabilistic characterisations of future seismicity. For each, damage accumulation at specific locations is calculated using the DAF methodology. On the available 18-processor workstation, such a simulation took one week of computational time, with the various timelines being evaluated in parallel. Aggregating these simulations, fragility-like curves are developed, with the horizontal axis representing time (years). Figure 17 compares these curves at the representative location of Loppersum (see Fig. 13).

The resulting curves clearly illustrate differences in damage exceedance probabilities and expected damage (Ψ) across scenarios. As anticipated, the two scenarios with reduced seismic activity produce correspondingly lower projected damage levels. Differences between scenarios, although modest, underscore the utility of the DAF approach in distinguishing potential outcomes based on varying seismic forecasts. However, the assessment of the scenarios reveals that a drastic reduction in seismicity would need to occur for damage progres-

Table 3 Three hypothetical scenarios for potential future seismicity distinguished by their mean yearly rate of events

Scenario	Initial Yearly Rate (year 0)	Final Yearly Rate (year 50)	Decrease
Continued	11.5	11.5	-
Reduced	11.5	½ · 11.5	linear
Stopped	11.5	0	linear

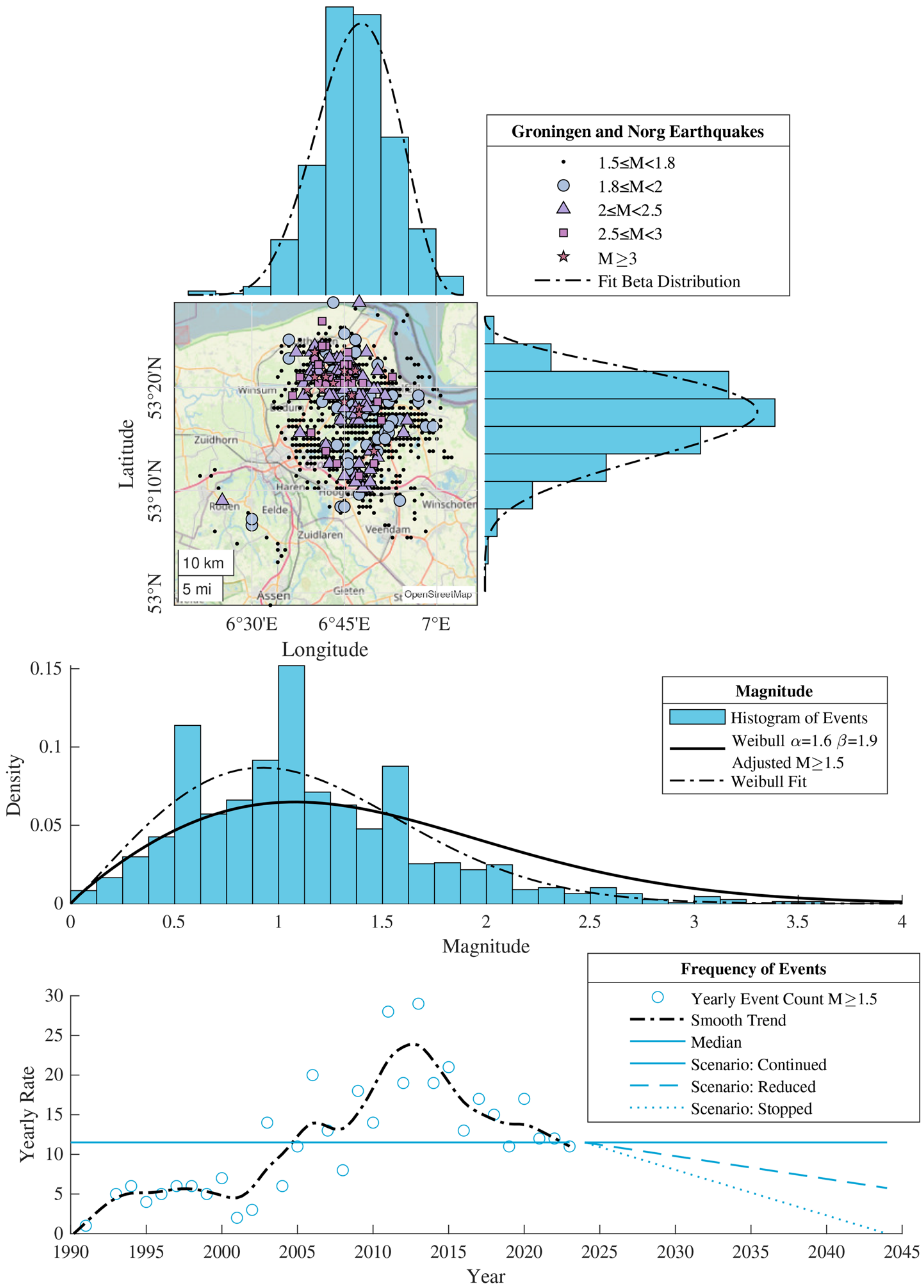

Fig. 16 Spatial distribution of historical seismic event epicentres (top panel) and Weibull distribution of event magnitudes, correlated latitude and longitude distributions, and projected annual frequency of events (bottom panel). Analyses are based on historical seismic data updated to March 2024. This data is used to formulate an empirical model for future scenarios. The adjusted Weibull fit considers only events with $M \geq 1.5$. The Weibull distribution was fitted with shape parameter $\alpha \approx 1.6$ and scale parameter $\beta \approx 1.9$; beta distributions for latitude ($\alpha \approx 6.84$, $\beta \approx 4.11$) and longitude ($\alpha \approx 6.77$, $\beta \approx 4.41$) were fitted to historical epicentre coordinates

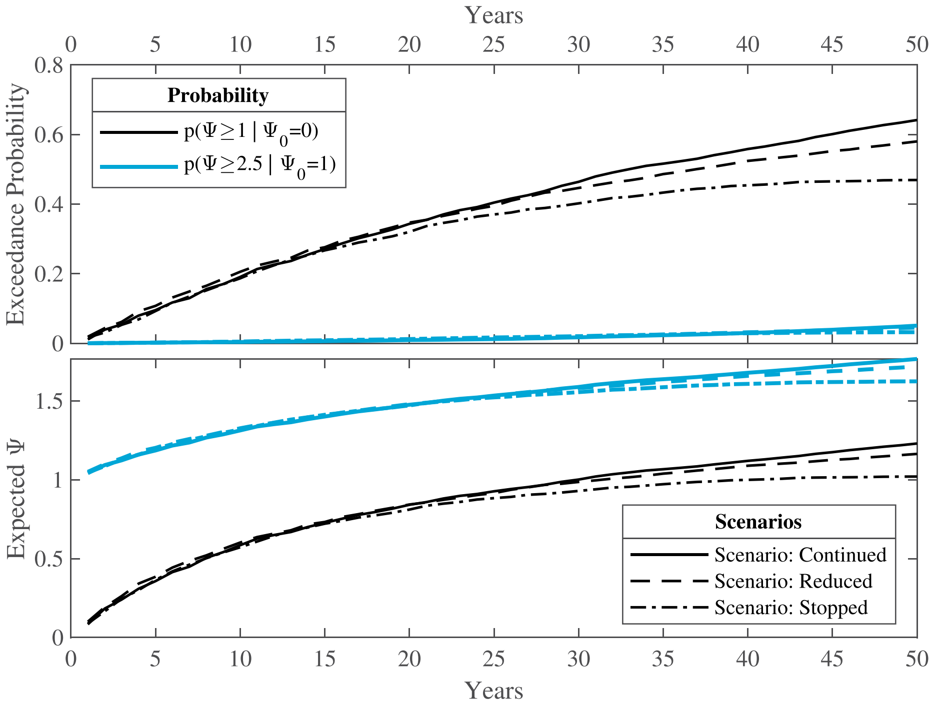

Fig. 17 Probability of damage over time: "fragility" curves for the various seismicity scenarios over the following 50 years. Top, exceedance probability, and bottom, expected damage for two damage thresholds corresponding to the beginning of DS1, with Ψ=1, and the end of light damage with Ψ=2.5

sion to be significantly affected. To date, the Dutch government has stopped the extraction of gas in the region (Toti et al. 2015).

7 Discussion

This study proposed a sequence-aware, crack-based Damage Accumulation Function (DAF) for light damage in URM that advances a measured state, Ψ, through arbitrary histories of PGV. Relative to conventional, event-wise workflows based on EMS-98 and typology fragilities (Lagomarsino et al. 2013; Grünthal et al. 1998; Lovon et al. 2018) or Groningen portfolio models that convolve induced-seismic hazard with fragility and consequence functions (Crowley et al. 2017, 2019; Lovon et al. 2018), the central advantage is that the DAF carries memory: it distinguishes similar-intensity repetitions (small increments) from "record-breaking" events (disproportionate jumps) and does so with an uncertainty scheme that grows with PGV yet avoids over-accumulating variance across long histories. In doing so, it codifies two Groningen observations from both experiments and modelling: many small, repeated events nudge visible cracks forward; a new maximum intensity produces a marked increase, $\Delta\Psi$.

A key strength is interpretability. Ψ is a physically motivated, measurable scalar that aggregates number, length and width of cracks and that has been shown to respond predictably under repeated drift at sub-percent levels, including direction-dependent degradation after one-way cycling. Using Ψ as the carried state variable allows a single metric to connect full-scale tests, NLTHA and field observations. The DAF is also compatible with Groningen inputs and practice: it accepts site PGV histories from region-specific GMPEs (Bommer et al. 2017; Atkinson 2015; Suzuki and Iervolino 2017), includes soil–foundation interaction following standard impedance concepts (Gazetas 1991) and the Groningen SSI framework (Longo et al. 2021), and can be run either on prescribed historical sequences (e.g., Fig. 1) or on simulated scenarios (e.g., Fig. 17) constrained by induced-seismicity bounds (Zöller and Holschneider 2016).

Although the FE models that generated the simulation pool are not re-developed within this paper, they are the empirical basis for the surrogate and, hence, for the DAF. A homogenised FEM constitutive modelling approach (EMM) was preferred to alternatives such as DEM (Malomo et al. 2018; Malomo and DeJong 2021) because it allowed thousands of runs to be performed quickly, robustly and reproducibly, with parameters that could be directly calibrated against DIC-based crack maps and force-drift loops. DEM can resolve masonry discontinuities in detail, but its parameter identification, contact calibration, and computational burden make it challenging to assemble the large, systematically varied pool required here and already available. The homogenised FEM strategy therefore provided the most practical route to a broad, Groningen-relevant dataset while still reproducing the crack-localisation patterns needed to define and carry Ψ. Nevertheless, this database could be expanded with additional geometries, soil profiles, and events/records.

Compared with other attempts to incorporate repetition, the DAF provides a general, transferable rule rather than case-specific cycle counting or degradation indices (Sarhosis et al. 2019; Grant et al. 2019). Against event-wise fragility approaches, DAF predictions better reconcile observed visible cracking after years of "small" shaking with calculations that would otherwise focus on a single largest event (Lagomarsino et al. 2013; Crowley et al. 2019). Against detailed NLFE sequence studies, the DAF offers scalability: once the surrogate $\Delta\Psi(\cdot)$ is fitted, long, heterogeneous histories can be evaluated probabilistically without rerunning high-fidelity FE for each site and sequence. The method also aligns with insights from adjacent domains such as settlement-induced façade damage (Burland and Wroth 1974; Prosperi et al. 2025) and infilled-frame cyclic deterioration (Filippou et al. 2019), that emphasise state tracking and sequence effects.

This paper also extracts the sequence-aware behaviour into a practical shorthand: a surface fit that maps the intensity of repeated PGV and the number of repetitions'n'to the expected fractional increase in damage relative to a single event at that PGV (Fig. 18). This quick-look estimator captures the broad DAF trends (modest increments for similar-intensity repeats and steepening at higher PGV) while remaining transparent enough for quick estimations without the complex analysis of entire PGV histories. It is intended strictly for the DS1 regime and within the calibration envelope. The surface is conservative for low PGV, reflects diminishing returns with increasing n, and makes explicit that repetitions rarely "double" damage unless both intensity and count are large; conditions under which light-damage assumptions may no longer hold. Quantitatively, the three line-cuts shown in the figure appear like poor fits and have an R^2 of approximately 0.50, 0.65, and 0.87 (from low to higher PGV slices); however, the underlying two-parameter surface (from which the slices are taken) achieves an R^2 of 0.93. The lower R^2 for lines reflects projection of a

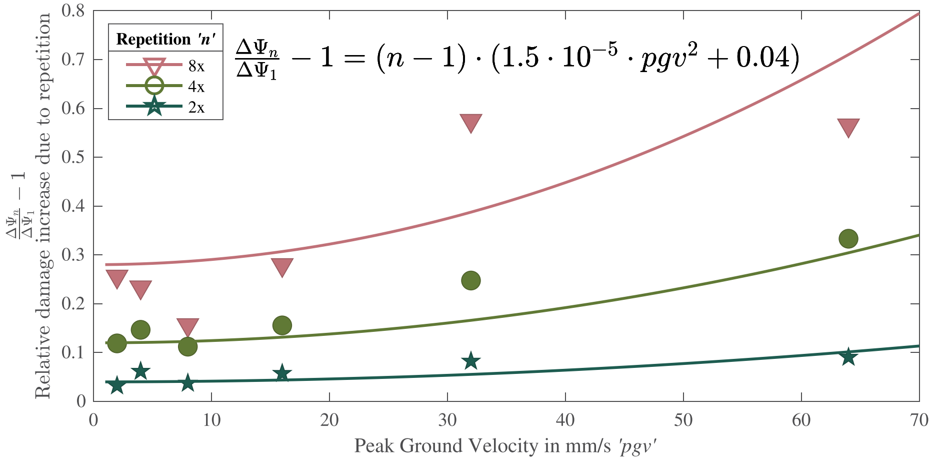

Fig. 18 Prediction of Ψ increase due to repetition. Simplified quadratic law that considers the number of repetitions n and the intensity of vibrations (PGV, mm/s) to estimate the expected percentile increase relative to the original event. Valid for light-damage (DS1) conditions and within the calibration range

surface onto 1D slices; as intended, the surface is a communication aid, not a substitute for the DAF when precise, sequence-specific estimates are required.

The applications in Sect. 3 demonstrate how the DAF ingests real or simulated PGV histories to produce sequence-aware damage predictions with uncertainty; the numerical outcomes are contingent on the scenario, parameter sampling and initial conditions used. Within this framing, "damage hastening" quantifies how repeated vibrations advance the timing of crack-damage realisation. These are concept demonstrations; for decisions, the DAF should be paired with site- and typology-specific inputs and, where available, validated against empirical damage data.

Experimental validation of the DAF could be an alternative. Full-scale dynamic tests of Groningen-type houses exist in the literature, but they typically target higher damage states and global response, with instrumentation and sampling rates not optimised for light-damage tracking at the spatial/temporal resolution required to evaluate Ψ. By design, the present work focuses on DS1 and leverages quasi-static, high-resolution DIC where minute crack increments are measurable and repeatable. Moreover, creating a surrogate for sequence analysis required a large, systematically varied pool of simulations. To calibrate DAF directly from full 3D building NLTHA that mirror shake-table tests, one would need orders of magnitude more computational effort; for example, a single 3D NLTHA of a house typology can require ~10 days per ground motion. Future work will confront the DAF against available dynamic building tests as more light-damage-focused instrumentation (e.g., high-speed, high-resolution DIC) becomes available and as computational resources make larger 3D pools feasible.

From the available experimental data, a strict one-to-one validation is neither possible nor intended from Figure 12 because different response quantities are shown on the y-axes: force reduction from displacement-controlled experiments versus ΔΨ from the DAF. The juxtaposition is interpretive: in the tests, stiffness loss at constant drift correlates with persistent crack widening/extension; in the DAF, ΔΨ formalises that accumulation. Groupings in the figure organise disparate but related evidence so that trends (small increments for similar-intensity repeats, larger jumps when demand rises, direction-dependence after prior cycling) can be read consistently across experiments, models and DAF outputs. The figure's role is thus to illustrate coherence of trends, not to show a strict quantitative match.

Furthermore, the curves in Figure 17 are "fragility-like" in that they show exceedance probabilities of damage states; they differ from classical fragility curves in using time (under a stochastic hazard process) on the horizontal axis rather than an intensity measure on a single event. This framing reflects the paper's central theme, that history matters, and communicates how different scenario assumptions change the trajectory of exceedance probabilities over time.

The present results are intentionally limited to the single typology investigated: single walls are used as proxies for façades. No explicit account is taken of multi-storey effects (global mode shapes, diaphragm participation, vertical load path and P–Δ amplification across storeys), of larger structural systems with many interacting wall elements (load redistribution, torsion, and damage migration at plan- or building-scale), of three-dimensional interactions (corner coupling, spandrel–pier interaction in real bays, diaphragm flexibility), or of out-of-plane behaviour (face-shell delamination, wythe interaction, rocking/slenderness). Likewise, floor typology (e.g., flexible timber vs stiff RC diaphragms), connection details (anchorage, ring beams), and the full breadth of masonry typologies (e.g., cavity walls, multi-wythe historic walls, diverse mortars/units beyond the calibrated fired-clay and selected CaSi sets) are not modelled explicitly. These omissions can be linked to future improvements. Yet the simplified approach is consistent with the aim: light, crack-based in-plane damage in representative wall-type components. While absolute damage is expected to change if these limitations are expanded, the relative increase in damage due to repetition is likely to be accurately reflected by the DAF.

Additionally, the parameter sensitivity analysis (Fig. 10) was conducted on homogeneous sequences, which allow systematic isolation of individual parameters (soil class, geometry, material). Extending this analysis to heterogeneous sequences would require disentangling parameter effects from sequence-ordering effects; this is deferred to future work.

Moreover, while the present formulation treats façades as in-plane systems and out-of-plane mechanisms, torsion at plan irregularities, or interaction with diaphragms are not modelled explicitly (D'Altri et al. 2020), other effects could also be relevant. For example, environmental and ageing effects (moisture, freeze–thaw, climate design (Kvande and Lisø 2009)) enter only indirectly via initial condition or parameter sampling. Likewise, settlement is considered via simple scenarios and parameter sets; explicit coupling of time-dependent ground movement with repeated seismicity would strengthen "damage hastening" estimates. Finally, empirical field validation at portfolio scale remains limited: while Figs. 13–15-type maps are internally consistent and mechanics-informed, systematic comparisons with inspection datasets would increase confidence in absolute exceedance probabilities (Messali et al. 2018; Esposito et al. 2019; Van Staalduinen et al. 2018).

Consequently, in practical applications beyond the calibration envelope, the DAF should be paired with (i) typology-specific parameter sets and intensity drivers (e.g., spectral velocity at T for different storey heights), (ii) system-level checks for 3D load paths and OOP stability, and (iii) sensitivity studies showing how diaphragm stiffness, wall density, and wythe configuration may alter $\Delta\Psi$.

Next, the method targets light, crack-based damage (DS1 and the lower edge of DS2). While appropriate for Groningen's frequent low-PGV sequences and for serviceability-level questions, it does not quantify capacity loss at higher states where failure mode and localisation dominate. Studies linking crack topology to residual stiffness/strength (Dolatshahi and Beyer 2022) and diagnostic frameworks (de Vent 2011; Latifi et al. 2023) suggest that augmenting Ψ with simple pattern descriptors (e.g., through-unit fractures, crack network connectivity, location with respect to openings) would improve inferences about post-event stiffness and usability. Second, the macro-constitutive model used for calibration (EMM) does not explicitly include cyclic degradation under many identical repeats; this is why within-step accumulation in the tests is under-represented in NLFE (Korswagen et al. 2019; Schreppers et al. 2016; Bindiganavile-Ramadas 2018; D'Altri et al. 2020). The DAF compensates at the methodology level via a calibrated similarity band and uncertainty, but constitutive upgrades would reduce model bias and sharpen the surrogate model.

Third, the DAF currently uses PGV as the intensity driver, consistent with Groningen short-period motions and the available GMPEs (Bommer et al. 2017; Atkinson 2015; Suzuki and Iervolino 2017). While practical, PGV alone does not encode duration or spectral shape. For façades whose first period T varies across the stock, alternative or compound drivers (e.g., spectral velocity at T, velocity-based energy measures, or simple duration modifiers) could improve sequence sensitivity without sacrificing interpretability. In addition, the choice of PGV aligns with Dutch practice: velocity-based criteria are used in vibration guidelines and in claims/administrative contexts, and velocity correlates more directly with energy content and drift demand in short-period, induced-seismic motions which are precisely the regime relevant to light, crack-based damage in masonry façades.

Fourth, the similarity ratio ρ that separates "repeat" from "record-breaking" updates (calibrated here around 0.25) is evidence-based but context-dependent; in practice it should be treated as a hyper-parameter and re-estimated per typology or intensity measure, with results reported alongside sensitivity bands whenever the DAF is applied beyond its calibration envelope. A principled route is Bayesian updating of ρ (and, if desired, of the similarity-band functional form) using staged or transitional Markov chain Monte Carlo (MCMC) so that posterior uncertainty and potential multi-modality (i.e., posteriors with multiple peaks) are made explicit (Beck and Au 2002; Green and Worden 2015). Several refinements could strengthen the uncertainty treatment in future work.

Fifthly, the current uncertainty scheme assumes that event-to-event dispersion is conditionally independent given the present state; long sequences may instead exhibit state-dependent correlation (e.g., progressive stiffness shifts altering T and SSI). A lightweight refinement is to endow the innovation with an autoregressive term whose coefficient depends on the evolving state (Ψ, PGV), or, more formally, to cast the evolution as a (partially observed) Markov process in which transitions depend on event intensity and a latent cumulative-damage variable (Rosenfield 1976). For richer data streams or when sequential inspections are available, sequential Bayesian filters/particle schemes can propagate the distribution of Ψ through long, heterogeneous histories at the expense of additional computation and modelling choices (Sun and Kumar 2012) (see also the MCMC roadmaps in Green & Worden (2015)). In short, Bayesian updating and Markovian formulations can strengthen the representation of uncertainty and temporal dependence in DAF-style analyses, but they introduce nontrivial costs (run-time, identifiability, prior specification, i.e., the assumed distributions before observing data) that should be weighed against the transparency and speed of the present formulation.

When considering damage hastening, the simulation exemplified here does not include maintenance or repairs that may have restored the capacity or decreased the damage of the structure. In addition, the effect of creep, which limits the appearance of damage when loads act slowly over an extended time period, is not considered either. Certain creep-based models can also consider accumulated damage (Tomor and Verstrynge 2013; Verstrynge et al. 2009), but not for repeated vibrations.

Taken together, the DAF should be viewed as a complement to established tools rather than a replacement. For rapid regional screening or consequence analysis, event-wise fragility remains efficient and transparent (Lagomarsino et al. 2013; Crowley et al. 2017, 2019). When the question is intrinsically historical or scenario-sequential: "What is the damage state today after decades of small events?"; "How much would different production curtailments change the trajectory?" the DAF fills the methodological gap by advancing a crack-based state through the actual or hypothesised sequence, with uncertainty that reflects Groningen variability.

8 Conclusions

This work develops a sequence-aware Damage Accumulation Function (DAF) for crack-based light damage in unreinforced masonry. The formulation advances a measured state or damage parameter, Ψ, through arbitrary histories of peak ground velocity (PGV), distinguishing between repetitions at comparable intensity and events that set a new maximum. Uncertainty is propagated with a PGV-dependent term whose incremental contribution diminishes along the sequence, preventing unrealistically broad prediction bands for long histories. The approach is grounded in previous full-scale experiments with high-resolution crack monitoring, calibrated macro-modelling, and nonlinear time-history analyses tailored to Groningen-type motions.

The main insight is that history matters: many small, repeated events produce modest but measurable increments in Ψ, whereas a new maximum intensity produces a disproportionate jump. The DAF captures both behaviours in a single, interpretable rule and provides a practical way to update damage state across heterogeneous sequences with explicit uncertainty. For screening and communication, a simplified two-parameter surface offers quick-look estimates of the expected fractional increase in damage as a function of PGV and the number of repeats, while the full DAF remains the tool of record for sequence-specific assessments. The main observation is that damage increases with every repetition, be it comparatively small or large.

Applications illustrate how the method can be used. Using observed PGV histories, the DAF tracks accumulation over decades at a location; extended to a grid, it produces regional exceedance maps that reflect spatial variability in shaking histories. The "damage hastening" construct shows how repeated vibrations can advance the timing of crack damage relative to other slow hazards. Scenario analyses demonstrate how alternative future seismicity trajectories translate into different time-evolving probabilities of light-damage exceedance, thus facilitating the comparisons of future scenarios.

The scope is intentionally focused. Results pertain to single walls used as proxies for façades and buildings in the light-damage regime (DS1 and early DS2). The scalar Ψ collapses pattern information and therefore should not be used to infer higher-state capacity loss without additional descriptors. The calibration backbone does not embed explicit cyclic-degradation laws for many identical repeats. PGV is used as the sole intensity driver and does not encode duration or spectral shape; the similarity ratio that separates “repeat” from “record-breaking” updates is calibrated for this context and may vary with typology. Multi-storey effects, system-level 3D interactions, diaphragm flexibility, out-of-plane mechanisms, and detailed floor/connection typologies are not modelled explicitly. Portfolio-scale empirical validation remains a priority.

These bounds suggest clear next steps. Methodologically, enrich Ψ with simple pattern metrics that carry information about crack topology; introduce explicit cyclic-degradation memory in the constitutive law; and test alternative or compound intensity measures that capture duration and period dependence. At system level, extend the calibration space to multi-storey façades, 3D assemblies with realistic diaphragms and connections, and out-of-plane stability checks. In multi-hazard settings, couple repeated seismic actions with time-dependent ground movements to quantify damage hastening more comprehensively. Finally, confront sequence-aware predictions with systematic inspection datasets to calibrate absolute exceedance levels at portfolio scale.

Within these limits, the DAF offers a transparent, scalable complement to event-wise practice. It carries state from one event to the next, respects order and intensity jumps, and provides a common language, Ψ, to connect experiments, models, mapping exercises, and decision-facing analyses wherever small earthquakes repeat often and light cracking is most relevant.

Acknowledgements The authors would like to acknowledge the support provided by NAM (Nederlandse Aardolie Maatschappij) and IMG (Instituut Mijnbouwschade Groningen) which was used to conduct the experiments in earlier work. The invaluable contribution of Dr. Edwin Meulman and Belen Gaggero (MSc) for the successful realisation of these experiments is also highlighted along with the support of laboratory staff at the TU Delft. In addition Dr. Karel Terwel provided feedback on several aspects of this work. Finally, thanks go to Michele Longo (MSc) for shaping the overall campaign with pre- and post-diction, and extrapolation numerical models. The results of these models were employed in this study.

Author contributions All authors contributed to the study conception and design. Data collection and analysis were performed by Paul Korswagen. The first draft of the manuscript was written by Paul Korswagen and all authors commented on previous versions of the manuscript. All authors read and approved the final manuscript.

Funding The authors declare that no funds, grants, or other support were received during the preparation of this manuscript.

Data availability The datasets comprising the model results which were analysed during the current study are available in the 4TU.ResearchData repository, http://doi.org/10.4121/58d1f5e6-5db3-4a74-a3d1-6e88a3bd8bce

Declarations

Competing interests The authors have no relevant financial or non-financial interests to disclose.

References

Amorosi A, Boldini D, De Felice G, Malena M, Sebastianelli M (2014) Tunnelling-induced deformation and damage on historical masonry structures. Géotechnique 64(2):118–130. https://doi.org/10.1680/geot.13.P.032

Atkinson GM (2015) Ground-motion prediction equation for small-to-moderate events at short hypocentral distances, with application to induced-seismicity hazards. Bull Seismol Soc Am 105(2a):981–992, April 2015. https://doi.org/10.1785/0120140142

Beck JL, Au S (2002) Bayesian updating of Structural models and Reliability using Markov Chain Monte Carlo simulation. J Eng Mech 128: 128(4(4):380–391. https://doi.org/10.1061/(ASCE)0733-9399(2002)128:4(380)

Bindiganavile-Ramadas S (2018) A hyperbolic model for degradation in tension mode-I fracture of masonry - implementation and validation in engineering masonry model. Delft University of Technology

Boelhouwer P, van der Heijden H (2018) The effect of earthquakes on the housing market and the quality of life in the province of Groningen, the Netherlands. J Hous The Built Environ 33(2):429–438. https://doi.org/10.1007/s10901-018-9600-y

Bommer JJ, Dost B, Edwards B, Kruiver PP, Ntinalexis M, Rodriguez-Marek A, Stafford PJ, van Elk J (2017) Developing a model for the prediction of ground motions due to earthquakes in the Groningen gas field. Neth J Geosciences - Geol en Mijnbouw 96(5):s203–s213. https://doi.org/10.1017/njg.2017.28

Burland JB, Wroth CP (1974) Settlement of buildings and associated damage. In Proceedings of Conference on Settlement of Structures, Pentech Press, Cambridge, 611–654

Chacara C, Reategui R, Ore Á, Suarez P, Aguilar R (2023) Integration of NDT, 3D Parametric modelling, and nonlinear numerical analysis for the seismic assessment of a vaulted Stone-masonry historical building. J Educ Chang Building Eng 70:106347. https://doi.org/10.1016/j.jobe.2023.106347

Cristiani D, Sbarufatti C, Giglio M (2021) Damage diagnosis and prognosis in composite double cantilever beam coupons by particle filtering and surrogate modelling. Struct Health Monit 20(3):1030–1050. https://doi.org/10.1177/1475921720960067

Crowley H, Pinho R, Polidoro B, van Elk J (2017) Developing fragility and consequence models for buildings in the Groningen field. Neth J Geosciences - Geol en Mijnbouw 96(5):s247–s257. https://doi.org/10.1017/njg.2017.36

Crowley H, Pinho R, Van Elk J, Uilenreef J (2019) Probabilistic damage assessment of buildings due to induced seismicity. Bull Earthquake Eng 17(8):4495–4516. https://doi.org/10.1007/s10518-018-0462-1

D'Altri AM, Sarhosis V, Milani G, Rots J, Cattari S, Lagomarsino S, Sacco E, Tralli A, Castellazzi G, de Miranda S (2020) Modeling strategies for the Computational Analysis of unreinforced masonry structures: review and classification. Arch Computat Methods Eng 27(4):1153–1185. https://doi.org/10.1007/s11831-019-09351-x

Dais D (2021) Monitoring, modelling and quantification of accumulation of damage on masonry structures due to recursive loads. The University of Leeds, School of Civil Engineering

Dais D, Bal İE, Smyrou E (2017) Discussion on the response of unreinforced masonry to low-amplitude RECURCIVE loads: case of Groningen gas field. In COMPDYN, 2017 Proceedings, 6th ECCOMAS

de Vent I (2011) Prototype of a diagnostic decision support tool for structural damage in masonry. Delft University of Technology, Faculty of Architecture. ISBN: 978-90-8570-760-8

Dolatshahi KM, Beyer K (2022) Stiffness and strength estimation of damaged unreinforced masonry walls using crack pattern. J Eart Eng 26(2):837–856. https://doi.org/10.1080/13632469.2019.1693446

Ennali N (2020) A comparison between the SLaMA method and NLFEA for 2D and 3D analyses of masonry structure. Delft University of Technology

Esposito R, Messali F, Ravenshorst GJP, Schipper HR, Rots JG (2019) Seismic assessment of a lab-tested two-storey unreinforced masonry dutch terraced house. Bull Earthquake Eng 17(8):4601–4623. https://doi.org/10.1007/s10518-019-00572-w

Esteva L, Díaz-López OJ, Vásquez A, León JA (2016) Structural damage accumulation and control for life cycle optimum seismic Performance of buildings. Struct Infrastruct Eng 12(7):848–860. https://doi.org/10.1080/15732479.2015.1064967

Filippou CA, Kyriakides NC, Chrysostomou CZ (2019) Numerical Modeling of masonry-infilled RC frame. TOBCTJ 13(1):135–148. https://doi.org/10.2174/1874836801913010135

Gao J, Du K, Qi J (2025) Quantifying the uncertainty of structural parameters using Machine Learning–based surrogate models. ASCE-ASME J Risk Uncertain Eng Syst Part A: Civ Eng 11(2):04025023. https://doi.org/10.1061/AJRUA6.RUENG-1550

García de Quevedo Inarritu P, Kohrangi M, Bazzurro P (2024) Damage assessment of unreinforced masonry buildings incorporating damage accumulation. Earthq Engng Struct Dyn 53(6):2122–2140. https://doi.org/10.1002/eqe.4106

Gazetas G. (1991) Formulas and charts for impedances of surface and embedded foundations. J Geotech Eng 117(9):1363–1381. https://doi.org/10.1061/(ASCE)0733-9410(1991)117:9(1363)

Giusto S, Cattari S, Lagomarsino S (2024) Investigating the reliability of nonlinear static procedures for the seismic assessment of existing masonry buildings. Appl Sci 14(3):1130. https://doi.org/10.3390/app14031130

Grant DN, Dennis J, Sturt R, McLennan D, Milan G, Huiu B, Palmieri M (2019) Explicit collapse prediction in the development of fragility Functions for an unreinforced masonry building with non-linear finite element models. SEDEC, Greenwich, London

Green PL, Worden K (2015) Bayesian and Markov Chain Monte Carlo Methods for identifying Nonlinear systems in the presence of uncertainty. Phil Trans R Soc A 373(2051):20140405. https://doi.org/10.1098/rsta.2014.0405

Grottoli L, Kallioras S, Korswagen P, Graziotti F (2019) In-plane and out-of-plane quasi-static cyclic tests on unreinforced calcium-silicate masonry walls under high compressive load. Technical report EUC067/2019U. EUCENTRE Foundation, Pavia, Italy. Available online at https://www.eucentre.it/nam-project

Grünthal G, Musson RMW, Schwarz J, Stucchi M (1998) European Macroseismic scale 1998 (EMS-98). European seismological commission, sub commission on engineering seismology, working group Macroseismic scales. In: Conseil de l'Europe, Cahiers du Centre Européen de Géodynamique et de Séismologie, vol 15. Luxembourg

Guerrini G, Kallioras S, Bracchi S, Graziotti F, Penna A (2021) Displacement demand for nonlinear static analyses of masonry structures: critical review and improved formulations. Buildings 11(3):118. https://doi.org/10.3390/buildings11030118

Gusella V (1998) Safety estimation method for structures with cumulative damage. J Eng Mech 124: 124(11(11):1200–1209. https://doi.org/10.1061/(ASCE)0733-9399(1998)124:11(1200)

https://wetten.overheid.nl/BWBR0046981/2023-07-01/2. May 2025

https://www.reuters.com/business/energy/dutch-senate-approves-law-permanently-close-groningen-gas-field-2024-04-16/. May 2025

Iervolino I, Giorgio M, Chioccarelli E (2016) Markovian modeling of seismic damage accumulation. Earthq Engng Struct Dyn 45(3):441–461. https://doi.org/10.1002/eqe.2668

Jafari S, Esposito R (2016) Material tests for the characterisation of replicated solid clay brick masonry. Report number C31B67WP1-12, version 01. 16 August 2017. Delft University of Technology

Katsimpini PS, Hatzigeorgiou GD, Beskos DE (2025) A damage Mechanics framework for In-plane seismic analysis of heritage masonry arch bridges under multiple events. Structures 80:110114. https://doi.org/10.1016/j.istruc.2025.110114

Korswagen P, Longo M, Meulman E, Rots JG (2019a) Experimental and computational study of the influence of pre-damage patterns in unreinforced masonry crack propagation due to induced, repeated earthquakes. In 13th North American Masonry Conference

Korswagen PA, Longo M, Meulman E, Rots JG (2019b) Crack initiation and propagation in unreinforced masonry specimens subjected to repeated in-plane loading during light damage. Bull Earthquake Eng 17(8):4651–4687. https://doi.org/10.1007/s10518-018-00553-5

Korswagen PA, Longo M, Rots JG (2020a) Calcium silicate against clay brick masonry: an experimental comparison of the in-plane behaviour during light damage. Bull Earthquake Eng 18(6):2759–2781. https://doi.org/10.1007/s10518-020-00803-5

Korswagen PA, Longo M, Rots JG (2020b) High-resolution monitoring of the initial development of cracks in experimental masonry shear walls and their reproduction in finite element models. Eng Struct 211:110365. https://doi.org/10.1016/j.engstruct.2020.110365

Korswagen PA, Longo M, Rots JG (2022) Fragility curves for light damage of clay masonry walls subjected to seismic vibrations. Bull Earthquake Eng 20(11):6193–6227. https://doi.org/10.1007/s10518-022-01404-0

Korswagen PA, Rots JG (2020) Monitoring and quantifying crack-based light damage in masonry walls with Digital image correlation. In Proceedings of 1st International Conference on Structural Damage Modelling and Assessment, Lecture Notes in Civil Engineering, pp 110). https://doi.org/10.1007/978-981-15-9121-1_1

Korswagen PA, Rots JG, Terwel KC (2025) Experimentally-based in-plane drift limits for the upper threshold of masonry light damage. Earthq Engng Struct Dyn 54(1):86–99. https://doi.org/10.1002/eqe.4246

Kvande T, Lisø KR (2009) Climate adapted design of masonry structures. Building Environ 44(12):2442–2450. https://doi.org/10.1016/j.buildenv.2009.04.007

Lagomarsino S, Cattari S (2013) Fragility functions of masonry buildings. In: Pitilakis K et al. (eds) SYNER-G: typology definition and fragility functions for physical elements at seismic risk, geotechnical, geological and earthquake engineering 27. https://doi.org/10.1007/978-94-007-7872-6_5

Latifi R, Hadzima-Nyarko M, Radu D, Rouhi R (2023) A brief overview on crack patterns, repair and strengthening of historical masonry structures. Materials 16(5):1882. https://doi.org/10.3390/ma16051882

Lepov VV (2013) Structural evolution model of damage accumulation processes in modern metallic and polymer nanomaterials. World J Eng 10(3):205–212. https://doi.org/10.1260/1708-5284.10.3.205

Li Z, Tao D, Li M, Shu Z, Jing S, He M, Qi P (2019) Prediction of damage accumulation effect of wood Structural members under long-term service: a machine learning approach. Materials 12(8):1243. https://doi.org/10.3390/ma12081243

Liu B, Kawabe D, Kim C, Sarhosis V (2024) Full life-cycle vibration-based monitoring of a full-scale masonry arch bridge with increasing levels of damage. Eng Struct 315:118466. https://doi.org/10.1016/j.engstruct.2024.118466

Liu B, Sarhosis V, Lemos JV (2024) Quantification of the crack propagation and global Failure mechanism of single- and multi-ring masonry Arch Bridges. Eng Struct 306:117805. https://doi.org/10.1016/j.engstruct.2024.117805

Liu Y, Sun B, Guo T, Li Z (2025) Multiscale damage analysis of engineering structures from material level to structural level: a systematic Review. IJSI 16(2):2025 pp. 275–310. https://doi.org/10.1108/IJSI-12-2024-0211

Longo M, Sousamli M, Korswagen PA, van Staalduinen P, Rots JG (2021) Sub-structure-based 'three-tiered' finite element approach to soil-masonry-wall interaction for light seismic motion. Eng Struct 245:112847. https://doi.org/10.1016/j.engstruct.2021.112847

Lovon H, Tarque N, Silva V, Yepes-Estrada C (2018) Development of fragility curves for confined masonry buildings in Lima, Peru. Earthquake Spectra 34(3):1339–1361. https://doi.org/10.1193/090517EQS174M

Lu Q, Zhu J, Zhang W (2020) Quantification of fatigue damage for structural details in slender coastal bridges using machine learning-based Methods. J Bridge Eng 25(7):04020033. https://doi.org/10.1061/(ASCE)BE.1943-5592.0001571

Luciano R, Sacco E (1998) A damage model for masonry structures. Eur J Mech Solids 17(2):285–303. https://doi.org/10.1016/S0997-7538(98)80087-9

Lutes LD, Corazao M, Hu S-LJ, Zimmerman J (1984) Stochastic Fatigue damage accumulation. J Struct Eng 110: 110(11(11):2585–2601. https://doi.org/10.1061/(ASCE)0733-9445(1984)110:11(2585)

Lv Z, Huang H, Zhu S, Gao H, Zuo F (2015) A modified Nonlinear Fatigue damage accumulation model. Int J Damage Mech 24(2):168–181. https://doi.org/10.1177/1056789514524075

Malomo D, DeJong MJ (2021) A macro-distinct element model (M-DEM) for simulating the in-plane cyclic behavior of URM structures. Eng Struct 227:111428. https://doi.org/10.1016/j.engstruct.2020.111428

Malomo D, DeJong MJ, Penna A (2018) Distinct element modelling of the In-plane Failure mechanisms of urm walls. In: 10th IMC. Milan

Massart TJ, Peerlings RHJ, Geers MGD (2007) Structural damage Analysis of masonry walls using Computational homogenization. Int J Damage Mech 16(2):199–226. https://doi.org/10.1177/1056789506064943

Melnikov B, Semenov A (2014) Fatigue damage accumulation under the complex varying loading. AMM 617:187–192. https://doi.org/10.4028/www.scientific.net/AMM.617.187

Mendes N, Lourenço PB (2015) Seismic Vulnerability of existing masonry buildings: nonlinear Parametric Analysis. Seismic Assess, Behav Retrofit Heritage Build Monuments, Comput Methods Appl Sci 37. https://doi.org/10.1007/978-3-319-16130-3_6

Messali F, Esposito R, Jafari S, Ravenshorst G, Korswagen PA, Rots JG (2018) A Multiscale experimental characterization of Dutch unreinforced masonry buildings. In 16th European Conference on Earthquake Engineering, Thessaloniki 2018

Messali F, Longo M, Singla A, Rots JG (2022) A Comparative Computational study on the static pushover and dynamic time history response of a masonry building. Comput Modell Concr Concr Struct. https://doi.org/10.1201/9781003316404-41

Mkrtychev O, Lokhova E (2021) Accumulation of damage in Reinforced Concrete elements under cyclic loads. IOP Conf Ser: Mater Sci Eng 1015(1):1015–012038. https://doi.org/10.1088/1757-899X/1015/1/012038

Mouyiannou A, Penna A, Rota M, Graziotti F, Magenes G (2014 June) Implications of cumulated seismic damage on the seismic Performance of unreinforced masonry buildings. BNZSEE 47(2):157–170. https://doi.org/10.5459/bnzsee.47.2.157-170

Mulder M, Perey P, Scholtens B, de Kam G, Perlaviciute G (2018 June) Gas production and earthquakes in Groningen - reflection on economic and social consequences. Cent Energy Econ Res - CEER - Policy Papers (3 2018

Nie P, Liu H, Wang Y, Han S (2024) Seismic response and Collapse Analysis of a transmission tower structure: assessing the impact of the damage accumulation effect. Buildings 14(7):2243. https://doi.org/10.3390/buildings14072243

Oyguc R, Tonuk G, Oyguc E, Ucak D (2023) Damage accumulation modelling of two Reinforced Concrete buildings under seismic sequences. Bull Earthquake Eng 21(10):4993–5015. https://doi.org/10.1007/s10518-023-01729-4

Prosperi A, Korswagen PA, Korff M, Schipper R, Rots JG (2023) Empirical fragility and ROC curves for masonry buildings subjected to settlements. J Educ Chang Building Eng 68:106094. https://doi.org/10.1016/j.jobe.2023.106094

Prosperi A, Longo M, Korswagen PA, Giardina G, Rots JG (2025) Comparative study of NLFE models for simulating settlement-induced damage in masonry façades: macro- and simplified micro-models. Front Built Environ 11:1618329. https://doi.org/10.3389/fbuil.2025.1618329

Rezaie A, Godio M, Achanta R, Beyer K (2022) Machine-Learning for damage assessment of rubble Stone masonry piers based on crack patterns. Automation Construct 140:104313. https://doi.org/10.1016/j.autcon.2022.104313

Rosenfield D (1976) Markovian deterioration with Uncertain information. Oper Res 24(1):141–155. https://doi.org/10.1287/opre.24.1.141

Samadian D, Muhit IB, Dawood N (2025) Application of data-driven surrogate models in Structural Engineering: a literature Review. Arch Computat Methods Eng 32(2):735–784. https://doi.org/10.1007/s11831-024-10152-0

Sandoval C, Valledor R, Lopez-Garcia D (2017) Numerical assessment of accumulated seismic damage in a historic masonry building. A case study. Int J Architectural Heritage 11(8):1–18. https://doi.org/10.1080/15583058.2017.1356945

Sangirardi M, Altomare V, De Santis S, de Felice G (2022) Detecting damage evolution of masonry Structures through computer-vision-based Monitoring Methods. Buildings 12(6):831. https://doi.org/10.3390/buildings12060831

Sarhosis V, Dais D, Smyrou E, Bal IE (2019a) Computational modelling of damage accumulation in unreinforced masonry Dutch constructions subjected to induced seismicity. In SECED Conference September 2019, Greenwich, London

Sarhosis V, Dais D, Smyrou E, Bal İE (2019b) Evaluation of modelling strategies for estimating cumulative damage on Groningen masonry buildings due to recursive induced earthquakes. Bull Earthquake Eng 17(8):4689–4710. https://doi.org/10.1007/s10518-018-00549-1

Sarhosis V, Dais D, Smyrou E, Bal İE, Drougkas A (2021) Quantification of damage evolution in masonry walls subjected to induced seismicity. Eng Struct 243:112529. https://doi.org/10.1016/j.engstruct.2021.112529

Schijve J (1972) The accumulation of Fatigue damage in aircraft Materials and Structures. AGARDograph No. 157

Schreppers GMA, Garofano A, Messali F, Rots JG (2016) DIANA validation report for masonry modelling. DIANA FEA report 2016-DIANA-R1601 143 pp TU Delft Structural Mechanics Report CM-2016-17

Shadlou M, Ahmadi E, Kashani MM (2020) Micromechanical modelling of mortar joints and brick-mortar interfaces in masonry Structures: a review of recent developments. Structures 23:831–844. https://doi.org/10.1016/j.istruc.2019.12.017

Shettya N, Livitsanos G, Van Roy N, Aggelis DG, Van Hemelrijck D, Wevers M, Verstrynge E (2019) Quantification of progressive Structural Integrity loss in masonry with Acoustic Emission-based damage Classification. Construct Building Mater 194:192–204. https://doi.org/10.1016/j.conbuildmat.2018.10.215

Shi Y, Pan Y, Wang S, Zhong W, Cui J (2024) Damage assessment method of clay brick masonry load-bearing walls under intense explosions with long duration. Eng Fail Anal 166:108830. https://doi.org/10.1016/j.engfailanal.2024.108830

Sokolkin YV, Vil'deman VE, Zaitsev AV, Rochev IN (1998 2) Structural damage accumulation and stable postcritical deformation of composite materials. Mech Compos Mater 34, No 2):171–183. https://doi.org/10.1007/BF02256036

Stroebe K, Kanis B, Richardson J, Oldersma F, Broer J, Greven F, Postmes T (2021) Chronic disaster impact: the long-term psychological and physical health consequences of housing damage due to induced earthquakes. BMJ Open 2021 11(5):e040710. https://doi.org/10.1136/bmjopen-2020-040710

Sun Y, Kumar M (2012) A Markov Chain Monte Carlo Particle solution of the initial uncertainty propagation problem. In AIAA Guidance, Navigation, and Control Conference AIAA 2012-4937. https://doi.org/10.2514/6.2012-4937

Suzuki A, Iervolino I (2017) Italian vs. worldwide history of largest PGA and PGV. Ann Geophysics 60(5):S0551. https://doi.org/10.4401/ag-7391

Tomor A, Verstrynge E (2013) A joint fatigue–creep deterioration model for masonry with acoustic emission based damage assessment. Construct Building Mater 43:575–588. https://doi.org/10.1016/j.conbuildmat.2013.02.045

Toti J, Gattulli V, Sacco E (2015) Nonlocal damage propagation in the dynamics of masonry elements. Comput Struct 152:215–227. https://doi.org/10.1016/j.compstruc.2015.01.011

van der Voort N, Vanclay F (2015) Social impacts of earthquakes caused by gas extraction in the province of Groningen, the Netherlands. Environ Impact Assess Rev 50(2015):1–15. https://doi.org/10.1016/j.eiar.2014.08.008

van Elk JF, Bourne SJ, Oates SJ, Bommer JJ, Pinho R, Crowley H (2019 January) A probabilistic model to evaluate options for mitigating induced seismic risk. Earthquake Spectra · 35(2):537–564. https://doi.org/10.1193/050918EQS118M

Van Staalduinen PC, Terwel K, Rots JG (2018) Onderzoek naar de oorzaken van bouwkundige schade in Groningen Methodologie en case studies ter duiding van de oorzaken. Report number CM-2018-01. 11 July 2018 - Downloadable from Delft University of Technology. https://www.NationaalCoordinatorGroningen.nl .

Vanniamparambil PA, Bolhassani M, Carmi R, Khan F, Bartoli I, Moon FL, Hamid A, Kontsos A (2014 11) A data fusion approach for progressive damage Quantification in Reinforced Concrete masonry walls. Smart Mater Struct 23(1):015007. https://doi.org/10.1088/0964-1726/23/1/015007

Verstrynge E, Schueremans L, Hendriks MAN (2009) Modeling of long-term deformations and damage accumulation in masonry. In Computational Modeling Workshop on Concrete, Masonry and on Fiber-reinforced Composites, Delft, The Netherlands. June 17–18, 2009

Wu B, Tang Y, Li Z, Tang K (2021) Fatigue damage accumulation modelling of Critical components subjected to moving crane loads in Reinforced-Concrete industrial buildings. Eng Fail Anal 119:104951. https://doi.org/10.1016/j.engfailanal.2020.104951

Wu Z, Fang G, Fu M, Chen X, Liang J, Lv D (2019) Random Fatigue damage accumulation Analysis of Composite thin-wall Structures based on residual stiffness method. Composite Struct 211:546–556. https://doi.org/10.1016/j.compstruct.2019.01.018

Yan S, Zou X, Ilkhani M, Jones A (2020) An efficient Multiscale surrogate modelling framework for Composite Materials considering progressive damage based on artificial neural networks. Compos Part B 194:108014. https://doi.org/10.1016/j.compositesb.2020.108014

Zhang P, Chen L, Wei T, Huang P, Wang H, Chen X (2024) Multi-hazard assessment of masonry buildings: a state-of-the-art Review. Buildings 14(12):3711. https://doi.org/10.3390/buildings14123711

Zhu S, Liu Q, Huang H (2017) Probabilistic Modeling of damage accumulation for Fatigue Reliability Analysis of railway axle steels. Procedia Struct Integrity 4:3–10. https://doi.org/10.1016/j.prostr.2017.07.012

Zöller G, Holschneider M (2016) The maximum possible and the maximum expected Earthquake magnitude for production-induced earthquakes at the gas field in Groningen, the Netherlands. Bull Seismol Soc Am 2016 106(6):2917–2921. https://doi.org/10.1785/0120160220